

Semi-boosted all-hadronic $t\bar{t}$ reconstruction performance on kinematic variables for selected BSM models using a 2D extesion of the BumpHunter algorithm

Jiří Kvita

Joint Laboratory of Optics of Palacký University and Institute of Physics AS CR, Faculty of Science, Palacký University, Olomouc, Czech Republic

E-mail: jiri.kvita@upol.cz

ABSTRACT: We explore the usage of boosted as well as semi-boosted topologies in all-hadronic $t\bar{t}$ final states in pp collisions at $\sqrt{s} = 14$ TeV, with one or both of the top quarks decaying into a boosted hadronic W -jet and an isolated b -jet. Correlations between selected kinematic variables and mass peak shapes of scalar and vector resonances decaying to a pair of top quarks are studied. Events corresponding to models with $t\bar{t}$ -associated production of invisible dark matter particle pairs are also generated and signal+background mixed samples are studied in terms of the ability to resolve an excess in the $t\bar{t}$ invariant mass, top quark p_T or other 1D and 2D spectra using a 2D extension of the BUMPHUNTER algorithm, resulting in an improved signal sensitivity. We identify the most promising variables with largest signal significance and possibly smaller sensitivity to experimental uncertainties like the jet calibration.

Contents

1	Introduction	1
2	Samples	2
3	Objects reconstruction	4
4	Event selection	5
5	Variables	9
5.1	Kinematic variables	9
5.2	Correlations between variables	10
5.3	Shape comparison	10
6	Results	14
6.1	Pseudo-data study	14
6.2	Replicas	14
6.3	Signal significance	14
7	Conclusions	18

1 Introduction

Search for the $t\bar{t}$ resonances have been performed by both the ATLAS ([1, 2]) and CMS ([3], also a search for a tW resonance [4]) experiments in both ℓ +jets and all-hadronic channels, setting limits for masses of beyond-the-standard model (BSM) Z' particles of various scenarios. The focus of this paper is not a study of non-excluded models, but rather the usage of generic scalar and vector resonance models to study possible improvements in reconstructing the $t\bar{t}$ kinematics in various topologies of the final state, namely regarding the degree of boost of the jets, and identify variables sensitive to the presence of a signal for the selected BSM models.

As the Large Hadron Collider (LHC) at CERN has provided a large dataset and current upgrade works aim increasing the center-of-mass energy as well as the luminosity, boosted topologies in hadronic final states are becoming heavily used tools in both measurements and searches at the LHC. They provide a handle on processes at large momentum transfer, with a chance of observing possible BSM signals.

One of the aims of this study is to employ the usage of events where a boosted W -like hadronic jets are reconstructed at medium traverse momenta, in order to study the enhancement of events between the traditional boosted topologies where the boosted jet mass and structure is consistent with a top-jet.

Shapes of several kinematic variables are studied at the particle and detector levels for the presence of a BSM signal in case of a scalar or vector particle decaying into a pair of top quarks, and for the case of an associated production of top quark pairs with a pair of invisible dark matter (DM) particles.

The signal significance is evaluated for various processes of the $t\bar{t}$ pair production at the central mass system energy of the pp system of 14 TeV, using the MADGRAPH5 event generator and the DELPHES parameterized detector simulation.

The presence of a signal peak or other modification of spectra is studied in boosted as well as semiboosted topologies, where, in the latter, one or two boosted jets consistent with the hadronic W candidate are identified, and the top quark candidates are formed by adding a four-momentum of the b -tagged jet. The purpose of this paper is not to optimize details of the W boson tagging algorithms but to explore these usually overlooked topologies in $t\bar{t}$ final states.

While searches for a concrete weak signal usually employ multivariate (MV) techniques to identify the phase space where the signal can be seen, searches for new physics often look into a single distribution like the invariant mass or missing transverse energy and do not select complicated phase space regions as details of new physics models can vary and shapes of distributions depend on particular model details like the width, mass and spin of a new resonance.

Cross-sections of SM processes are often fitted using simultaneous likelihood fits over many binned variables with detector and modelling systematic uncertainties being allowed to vary and be fitted (profiling). In contrast, in searches for new physics, limits are often set based on a 1D variable using an excess of events over a simulated, (semi) data-driven or fitted background, often validated in control regions, less often based on a MV discriminant due to model dependencies.

We propose an intermediate approach, selecting pairs of variables with a known small correlation in order to quantify a 2D excess of events over the expected background. We suggest dimensionfull as well as dimensionless variables and their pairs as 2D spectra for search for model BSM signals.

2 Samples

Using the MADGRAPH5 version 2.6.4 simulation toolkit [5], proton-proton collision events at $\sqrt{s} = 14$ TeV were generated for the SM process $pp \rightarrow t\bar{t}$ and for the resonant s -channel $t\bar{t}$ producing via an additional narrow-width (sub-GeV) vector boson Z' as $pp \rightarrow Z' \rightarrow t\bar{t}$ (using the model [6–8]). These samples were generated in the all-hadronic $t\bar{t}$ decay channel and at next-to-leading order (NLO) in QCD in production, using the MLM matching [9], *i.e.* with additional processes with extra light-flavoured jets produced in the matrix element, matched and resolved for the phase-space overlap of jets generated by the parton shower using MADGRAPH5 defaults settings. The parton shower and hadronization were simulated using PYTHIA8 [10]. Masses of the hypothetical Z' particle, serving effectively as a source of semi-boosted and boosted top quarks, were selected as 750, 800, 900, 1000, 1250 and 1500 GeV. In addition, also a model with a scalar particle decaying to a pair of

top quarks $y_0 \rightarrow t\bar{t}$ was adopted [7] at the leading-order (LO) in the $t\bar{t}$ production with the gluon-gluon fusion loop (more details in [11–18]), with inclusive $t\bar{t}$ decays, selecting the all-hadronic channel later in the analysis. As the last BSM process considered, the possibility of generating a pair of invisible dark matter (DM) fermions χ_D in association with a $t\bar{t}$ pair using the scalar y_0 particle as a mediator was also studied. For the scalar model, the probed masses were set to $m_{y_0} = 1000$ GeV with its natural width chosen as $\Gamma_{y_0} = 10, 100$ and 300 GeV, and for the associated production of the DM particles masses $m_{y_0} = 1000$ GeV, and $m_{\chi_D} = 10, 100$ and 300 GeV, all with $\Gamma_{y_0} = 10$ GeV were used. The mass of the top quark was set to 173 GeV (MADGRAPH5 default). A selection of representative MADGRAPH5 processes are depicted as Feynman diagrams in Figure 1 while the cross-sections and numbers of generated events for the considered processes are listed in Table 1. As typical background processes, the production of hadronically decaying W^\pm bosons in association with a $b\bar{b}$ pair, accompanied by up to two additional light-flavoured jets produced at the matrix element level, was also simulated using the MLM matching with the PYTHIA8 parton shower using MADGRAPH5 default settings and referred to as $Wbbjj$, and also the production of two W bosons decaying hadronically, accompanied by a $b\bar{b}$ pair at LO, referred to as $WWbb$.

The multijet background samples are not simulated as in practice they are determined by data-driven techniques in control regions in real data based on vetoing top-tagged jets. In a similar way, this background could be determined for the semi-boosted topologies detailed in Section 4 by considering also the W -tag veto regions. We do not develop novel data-driven techniques for the multijet background estimation but rather study new physics signals appearance and its shape properties above flat enough SM backgrounds from $t\bar{t}$ or hadronic W processes.

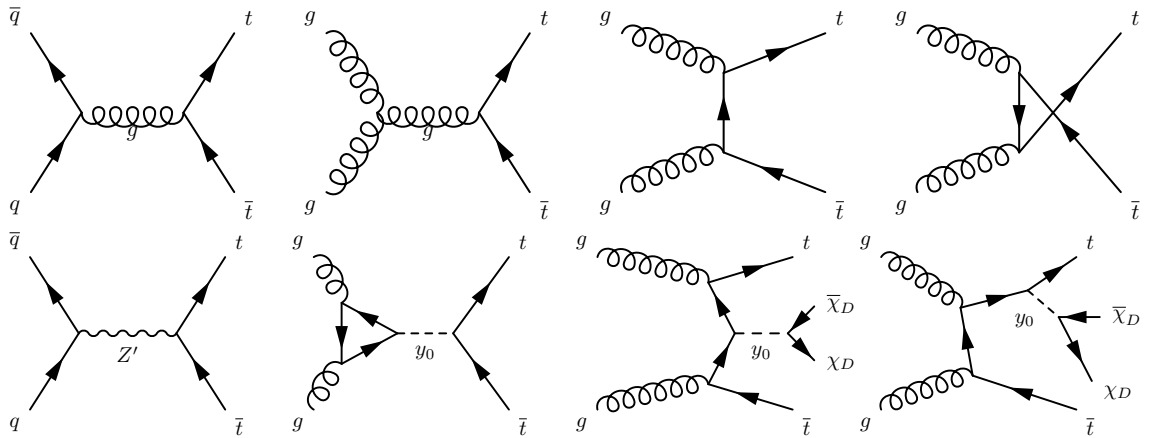


Figure 1. Dominant leading-order Feynman diagrams for SM (top) and selected BSM (bottom) processes of the $t\bar{t}$ pair production. Created using the *FeynMf* package [19].

Sample	Order	Parameters, comment	Events	Cross-section
$pp \rightarrow t\bar{t}(j) \rightarrow \text{hadrons}$ $60 \text{ GeV} < p_T^{j1,j2}$	NLO	$m_t = 173 \text{ GeV}$, matched control sample	5,283,343	309 pb
$pp \rightarrow t\bar{t}(j) \rightarrow \text{hadrons}$ $200 \text{ GeV} < p_T^{j1,j2}$	NLO	$m_t = 173 \text{ GeV}$, matched	1,841,859	7.0 pb
$pp \rightarrow t\bar{t}(j) \rightarrow \text{hadrons}$ $60 \text{ GeV} < p_T^{j1,j2} < 200 \text{ GeV}$	NLO	$m_t = 173 \text{ GeV}$, matched	1,896,629	271 pb
$pp \rightarrow t\bar{t}(j) \rightarrow \text{hadrons}$ $200 \text{ GeV} < p_T^{j1} < 60 \text{ GeV}$	NLO	$m_t = 173 \text{ GeV}$, matched	1,544,855	30 pb
$pp \rightarrow Z' \rightarrow t\bar{t}(j) \rightarrow \text{hadrons}$	NLO	$m_{Z'} = 750 \text{ GeV}$, matched	293,402	0.403 fb
$pp \rightarrow Z' \rightarrow t\bar{t}(j) \rightarrow \text{hadrons}$	NLO	$m_{Z'} = 800 \text{ GeV}$, matched	289,892	0.350 fb
$pp \rightarrow Z' \rightarrow t\bar{t}(j) \rightarrow \text{hadrons}$	NLO	$m_{Z'} = 900 \text{ GeV}$, matched	284,500	0.267 fb
$pp \rightarrow Z' \rightarrow t\bar{t}(j) \rightarrow \text{hadrons}$	NLO	$m_{Z'} = 1000 \text{ GeV}$, matched	279,442	0.206 fb
$pp \rightarrow Z' \rightarrow t\bar{t}(j) \rightarrow \text{hadrons}$	NLO	$m_{Z'} = 1250 \text{ GeV}$, matched	215,290	0.113 fb
$pp \rightarrow Z' \rightarrow t\bar{t}(j) \rightarrow \text{hadrons}$	NLO	$m_{Z'} = 1500 \text{ GeV}$, matched	261,620	0.0660 fb
$pp \rightarrow y_0 \rightarrow t\bar{t}$ incl.	loop SM	$m_{y_0} = 1000 \text{ GeV}$, $\Gamma_{y_0} = 10 \text{ GeV}$	1,000,000	305 fb
$pp \rightarrow y_0 \rightarrow t\bar{t}$ incl.	loop SM	$m_{y_0} = 1000 \text{ GeV}$, $\Gamma_{y_0} = 100 \text{ GeV}$	500,000	31.1 fb
$pp \rightarrow y_0 \rightarrow t\bar{t}$ incl.	loop SM	$m_{y_0} = 1000 \text{ GeV}$, $\Gamma_{y_0} = 300 \text{ GeV}$	500,000	10.0 fb
$pp \rightarrow y_0 t\bar{t} \rightarrow \chi_D \bar{\chi}_D t\bar{t} \rightarrow \text{hadr.}$	LO	$m_{y_0} = 1 \text{ TeV}$, $\Gamma_{y_0} = 10 \text{ GeV}$ $m_{\chi_D} = 10 \text{ GeV}$	500,000	2.44 fb
$pp \rightarrow y_0 t\bar{t} \rightarrow \chi_D \bar{\chi}_D t\bar{t} \rightarrow \text{hadr.}$	LO	$m_{y_0} = 1 \text{ TeV}$, $\Gamma_{y_0} = 10 \text{ GeV}$ $m_{\chi_D} = 100 \text{ GeV}$	1,000,000	2.29 fb
$pp \rightarrow y_0 t\bar{t} \rightarrow \chi_D \bar{\chi}_D t\bar{t} \rightarrow \text{hadr.}$	LO	$m_{y_0} = 1 \text{ TeV}$, $\Gamma_{y_0} = 10 \text{ GeV}$ $m_{\chi_D} = 300 \text{ GeV}$	500,000	1.24 fb
$Wbbjj \rightarrow \text{hadr.}, p_T^{j1,j2} > 60 \text{ GeV}$	LO	matched 0–2 additional jets	617,952	144 pb
$WWbb \rightarrow \text{hadr.}, p_T^{j1,j2} > 60 \text{ GeV}$	LO		2,000,000	126 pb

Table 1. Cross sections and numbers of events for the samples used, generated with MADGRAPH5+PYTHIA8, with cuts on the transverse momentum of the leading and sub-leading jets indicated as $j1$ and $j2$, respectively.

3 Objects reconstruction

Using the DELPHES (version 3.4.1) detector simulation [20] with a modified ATLAS card, jets with two distance parameters 0.4 and 1.0 were reconstructed using the anti- k_t algorithm to form corresponding small- R and large- R jets, using the FastJet algorithm [21] at both particle and detector levels. The DELPHES card was also modified to remove the DM particles from both detector jet clustering as well as from the particle jets.

Although no additional pp interactions (pile-up) were added to the simulated hard-scatter processes, the trimming jet algorithm [22] as part of the DELPHES package was used to obtain jets at both the particle and detector levels with removed soft components, using the parameter of $R_{\text{trim}} = 0.2$ and modified p_T fraction parameter $f_{\text{trim}}^{\text{PT}} = 0.03$ (originally 0.05). The trimming algorithm was chosen over the standard non-groomed jets, soft-dropped [23] and pruned jets [24], with parameters varied, in terms of the narrowness of the mass peaks. The jet masses shapes of the other algorithms differed in the expected peak positions at W and t masses, although they performed similarly and could be also tuned for the purpose of this analysis. In detail, in the default settings the W and top mass

peaks were shifted to higher values by 10–20 GeV, with a worse shape and shift for the W case which is important for the semiboosted regimes. The new settings help establish both the peaks shape as well as position at the expected values. While the new $t\bar{t}$ invariant mass distribution for the Z' sample with $m_{Z'} = 1$ TeV shifts down by about 50 GeV, the relative peak resolution remains the same.

This procedure leads to a more pronounced reconstructed W as well as top-quark mass peaks in terms of corresponding candidate large- R jet masses, and also to better correlation between the detector and particle levels for derived quantities like the transverse momentum of the top quarks or the $t\bar{t}$ invariant mass.

Custom jet energy scale (JES) correction was applied to large- R jets at the detector level, resulting in an up-scaling correction of 5–15% depending on η and p_T . Additional custom JES was applied also to the default DELPHES JES for small- R jets, resulting in additional correction of 5% in central rapidities and 4% at low p_T . JES closure tests in terms of the ratio of the particle and angularly matched detector-level jet result in agreement within 2%.

The jet subjetiness variables [25] τ_k , $k = 1, 2, 3$, and their ratios $\tau_{ij} \equiv \tau_i/\tau_j$ were employed as provided by the DELPHES jet reconstruction properties together with a simple selection on the large- R jet mass to identify jets coming from the hadronic decays of the W boson or a top quark. The large- R jets were tagged as

- W -jets if $0.10 < \tau_{21} < 0.60 \wedge 0.50 < \tau_{32} < 0.85 \wedge m_J \in [70, 110]$ GeV;
- top-jets if $0.30 < \tau_{21} < 0.70 \wedge 0.30 < \tau_{32} < 0.80 \wedge m_J \in [140, 215]$ GeV.

Illustrated in Figure 2 for the Z' sample with $m_{Z'} = 1$ TeV there are the correlations between the substructure variables and the large- R jet mass, demonstrating the small correlation between τ_{21} and τ_{32} but also the worse jet mass resolution at the detector as compared to the particle level.

The above definitions result in the W -tagging efficiency of about 0.6 in the jet p_T range of [150, 350] GeV with mistag rate of about 0.4; and to the top-tagging efficiency of about 0.6 in the jet p_T range of [150, 350] GeV with mistag rate below about 0.2; with numbers quoted for the $t\bar{t}$ sample, while for the Z' samples the top mistag rate is higher for $p_T < 600$ GeV than in the $t\bar{t}$ samples and falls again towards the high p_T .

The b -jets at the detector level were used as provided by the tagging efficiency in the default DELPHES ATLAS card, while for studies at the particle level, custom tagging based on the presence of a B hadron angularly close to the particle jet was implemented, using B hadrons with $p_T > 5$ GeV. Particle-level jets were tagged as b -jets if such a B hadron was within $\Delta R = \sqrt{(\Delta\eta)^2 + (\Delta\phi)^2} < 0.4$. Further, in order to account for the practically important case of falsely b -tagged jets, a custom random mistagging with a rate of 1% was added for originally non- b -tagged jets.

4 Event selection

Two classes of boosted large- R -jets are probed for appearance in events, either top-jets, *i.e.* jets with a mass and substructure consistent with the hypothesis that the top quark decay

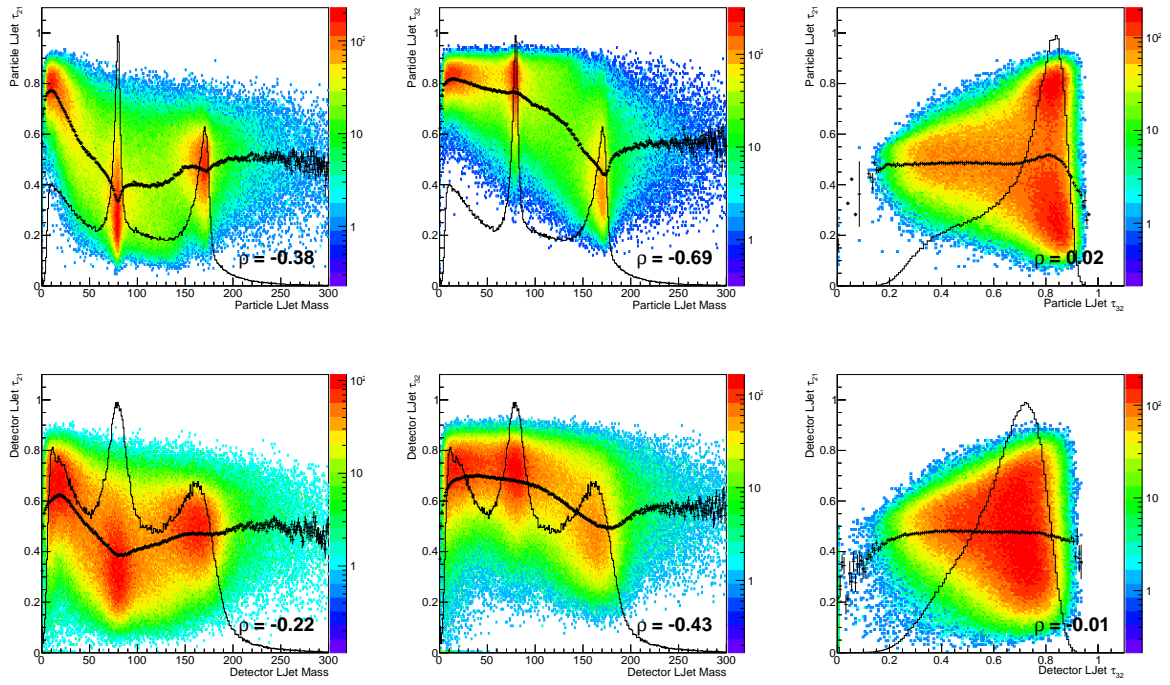


Figure 2. The τ_{21} (left) and τ_{32} (middle) jet structure variables plotted versus the large- R jet mass and the τ_{21} vs. τ_{32} for the Z' sample with $m_{Z'} = 1$ TeV at the particle (top) and detector (bottom) levels. The cross markers are the profile histogram while the solid line stands for the (scaled) projection of the histogram to the x axis. Also indicated is the standard correlation factor ρ .

products were reconstructed in such a large- R jet, or W -jets, *i.e.* those consistent with the hadronic decay of a W boson. We denote the top-like large- R jets as boosted (B), and the W -like jets as semiboosted (S). Based on their number in the event, we define in total three topologies of the all-hadronic $t\bar{t}$ final state denoted as the boosted-boosted (2B0S), boosted-semiboosted (1B1S) or semiboosted-semiboosted (0B2S), depicted in Figure 3 or as DELPHES event display examples in Figure 4. We do not pursue the resolved topology with dedicated techniques needed to study the combinatorics of ≥ 6 small- R jets. The fraction of the considered topologies as a function of the generated mass of the Z' vector boson are shown in Figure 5, together with the migration rate between the topologies at the particle and detector levels, in order to check the stability of the topologies concept at both levels. The migration is observed to be at the level of 10% in terms of the fraction of events migrating to different topologies. One can see that while the fractions of semiboosted topologies (1B1S and 0B2S) decrease with the mass of the resonance, they still constitute non-negligible fractions of 10–20% at medium masses of Z' , and about 30% for the SM $t\bar{t}$ sample.

The same event selection applied at the particle and detector levels can be summarised as follows:

- require at least two large- R jets with $p_T > 80$ GeV and $|\eta| < 2.0$;

- preselect small- R jets with $p_T > 25$ GeV and $|\eta| < 2.5$;
- require at least two small- R jets tagged as b -jets;
- reject events with an isolated high- p_T lepton above 25 GeV, in order to remove events from the $pp \rightarrow y_0 \rightarrow t\bar{t}$ for which, due to the triangle loop in the corresponding diagrams, the $t\bar{t}$ decay mode could not be specified at the generator level.
- Finally, attempt, in this order, the boosted-boosted (2B0S), boosted-semiboosted (1B1S) or semiboosted-semiboosted (0B2S) topologies reconstruction of the $t\bar{t}$ final state by requiring the corresponding numbers of top-tagged and W -tagged jets.

An example of the resulting detector-level yields for the Z' model in the 1B1S topology is listed in Table 2.

1B1S topology	Events yield	Weighted yeild	Stat. unc.
$Z' \rightarrow t\bar{t}, m_{Z'} = 1$ TeV($\times 10000 \times 2^{2.0}$)	6600 ± 81	15600 ± 190	1.2%
$t\bar{t}, p_T^{j1} \geq 200$ GeV $p_T^{j2} \in (60, 200)$ GeV	31500 ± 180	39600 ± 220	0.6%
$t\bar{t}, p_T^{j1,j2} \geq 200$ GeV	54800 ± 230	17400 ± 74	0.4%
$t\bar{t}, 60$ GeV $\leq p_T^{j1,j2} \leq 200$ GeV	3600 ± 60	50700 ± 840	1.7%
$WWbb, p_T^{j1,j2} > 60$ GeV	9000 ± 95	45500 ± 480	1.1%
$Wbbjj, p_T^{j1,j2} > 60$ GeV	530 ± 23	3900 ± 170	4.3%
pseudodata	105800	173500	
prediction	106100 ± 330	172700 ± 1000	0.6%
pseudodata / prediction	1.00	1.00	

Table 2. Unweighted and cross-section weighted event yields for the $t\bar{t}$ and non- $t\bar{t}$ background samples and the vector Z' model with $m_{Z'} = 1000$ GeV.

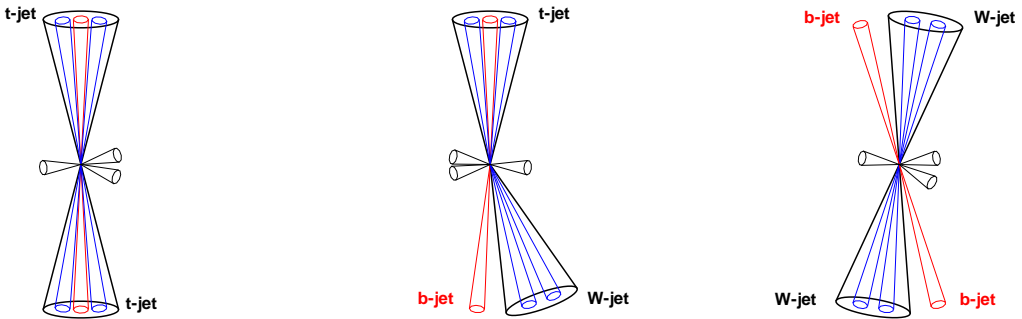


Figure 3. Cartoons of the event topologies, from left to right: 2B0S (boosted-boosted), 1B1S (boosted-semiboosted) and 0B2S (semiboosted-semiboosted). The large- R jets are shown as bold black large cones, sub-jets in blue while the b sub-jets in red, additional jets as black cones of small radii.

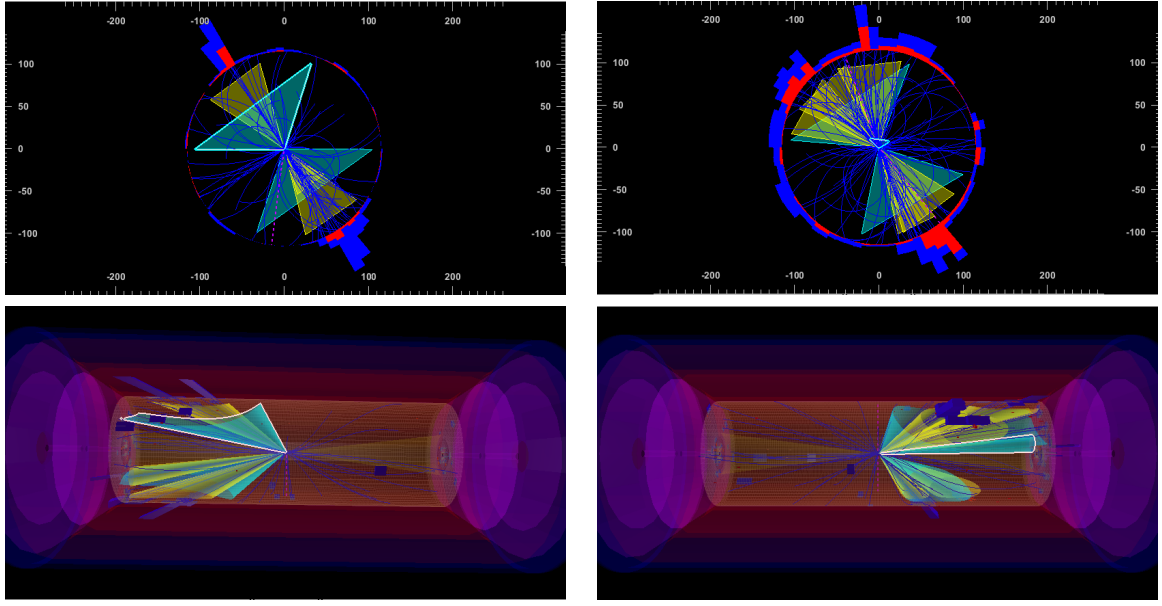


Figure 4. The DELPHES event display of a boosted $t\bar{t}$ event (left) and a more complex final state, namely additional jet activity (right), from the Z' sample with $m_{Z'} = 1$ TeV. Small- R (large- R) jets are depicted as yellow (light blue) cones. Also shown are tracks of charged particles as well as electromagnetic (red) and hadronic (blue) calorimeter energy deposits.

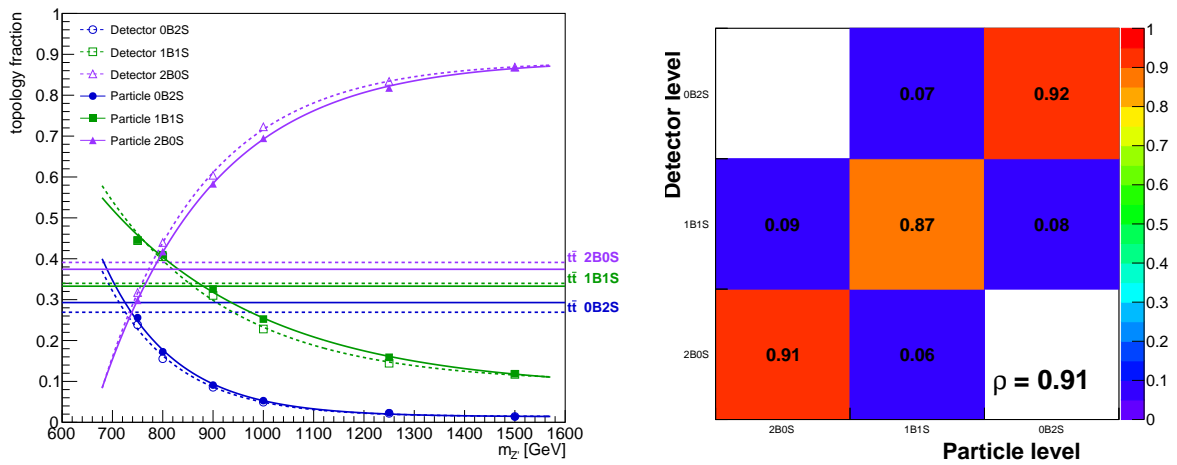


Figure 5. Left: Fractions of the 2B0S, 1B1S and 0B2S topologies in various samples as function of the Z' mass. The guiding lines are exponential fits, horizontal lines mark the fractions for the $t\bar{t}$ control sample. Both particle-level (solid lines, full markers) and detector-level (dashed lines, open markers) fractions are plotted. Right: Migration between the selection topologies at the particle and DELPHES detector levels with the overall correlation coefficient ρ indicated.

5 Variables

5.1 Kinematic variables

Typical variables studied in the $t\bar{t}$ system for SM precision differential cross-section measurements are the transverse momenta of the two top quarks (both used in this study, with event weights of 0.5), rapidity of the top quarks (y^t) and of the $t\bar{t}$ system ($y^{t\bar{t}}$), and the mass ($m^{t\bar{t}}$) and transverse momentum ($p_T^{t\bar{t}}$) of the $t\bar{t}$ system; their 2D and 3D extensions and variables related to additional jet activity in the event. Further variables are composed from the two top quarks momenta, like the $\cos\theta^*$ (angle between a top quark and the z axis in a frame where the $t\bar{t}$ system has zero momentum along the z axis), the laboratory opening angle between the two top quarks ($\delta_{t\bar{t}}$) and the $\Delta\phi$ between the two top quarks in the transverse plane ($\Delta\phi^{t\bar{t}}$). Other studied observables are the out-of-plane momentum p_{out} based on the direction of one of the top quarks defining a plane together with the beam (z axis) direction \hat{z} , to which the momentum of the other top quark is projected; and the $y_{\text{boost}}^{t\bar{t}}$ and $\chi^{t\bar{t}}$ variables, defined as

$$p_{\text{out}} \equiv \vec{p}^{t,2} \cdot \frac{\vec{p}^{t1} \times \hat{z}}{|\vec{p}^{t,1} \times \hat{z}|}, \quad \text{and } 1 \leftrightarrow 2 \quad (5.1)$$

$$y_{\text{boost}}^{t\bar{t}} \equiv \frac{1}{2} |y^{t2} + y^{t1}| \quad (5.2)$$

$$\chi^{t\bar{t}} \equiv \exp |y^{t2} - y^{t1}|. \quad (5.3)$$

These are sensitive to final state radiation, the boost of the $t\bar{t}$ system and thus also to parton distribution functions; and to new physics via their sensitivity to the production angle in the central-mass-system. We also study the ratio of the two top quark transverse momenta, $R^{t1,t2}$, the ratio of the leading to sub-leading top quark p_T . One can also use event shape variables (originally studied in QCD jet physics) based on the normalized momentum tensor defined using the three-momenta of objects \mathcal{O} in the event (usually jets) as

$$\mathcal{M}_{ij} \equiv \frac{\sum_{\mathcal{O}} p_i^{\mathcal{O}} p_j^{\mathcal{O}}}{\sum_{\mathcal{O}} (\vec{p}^{\mathcal{O}})^2} \quad (5.4)$$

where i, j run over the three space indices. The matrix has eigenvalues $\lambda_1 \leq \lambda_2 \leq \lambda_3$ used to define aplanarity $\mathcal{A} \equiv \frac{3}{2}\lambda_1$ and sphericity $\mathcal{S} \equiv \frac{3}{2}(\lambda_1 + \lambda_2)$. Corresponding aplanarity and sphericity for the small- R jets were studied, labelled as \mathcal{A}^j and \mathcal{S}^j in plots. Other global variables are also studied, namely

- the sum of p_T of small- R jets H_T^j ;
- missing transverse energy E_T^{miss} ; and the sum of $H_T^j + E_T^{\text{miss}}$;
- the sum of masses of large- R jets $\sum_J m_J$, labelled also as Sum m_J in plots;
- and the invariant masses of the 4-vector sum of large- R jets 4-momenta $m_{\sum J}^{\text{vis}}$, labelled also as $m_{\text{Sum}J}^{\text{vis}}$ in plots;

motivated by the fact that invisible BSM particles carrying significant transverse momentum can exhibit tails in E_T^{miss} , p_{out} , or contribute to higher jet activity in the event due to larger energy scale of events with production of high-mass particles. We keep the global event shape variables like aplanarity, sphericity; and H_T only for small- R jets while the jet-mass related quantities for larger- R jets.

In addition, dimensionless variables with potential of possessing smaller experimental uncertainties in absolute jet energy scale calibration were studied by constructing ratios relative to $m^{t\bar{t}}$ or to the geometric mean of the two top quark transverse momenta $\sqrt{p_T^{t1} p_T^{t2}}$.

5.2 Correlations between variables

Besides the obvious anti-correlations of variables to the relative quantities w.r.t. to such variables, and the negative correlation of $\Delta\phi^{t\bar{t}}$ to $p_T^{t\bar{t}}$ and p_{out} by construction, one can make several non-trivial observations. Out of all the variables especially p_{out} (or an absolute value of it) is a very useful one as it has only a small correlation to $m^{t\bar{t}}$ (we observe 0.07 for the $t\bar{t}$ control sample, see also Figure 6) while it exhibits a large shape change especially in tails for models with additional DM particles produced, see Figure 8. It has also been used for MC generators tuning as it is sensitive to the initial and final state radiation [26] while caution should be taken in order not to tune to possible new physics effects. We keep variables even with large absolute correlations for detailed study of their performance in terms of a signal significance. Both p_T^t and $p_T^{t\bar{t}}$ have large correlation to variables quantifying the jet p_T activity in the event like H_T^j and the total large- R jets visible mass $m_{\sum j}^{\text{vis}}$. There are also large negative correlations of sphericity and $y_{\text{boost}}^{t\bar{t}}$ to $m^{t\bar{t}}/\sqrt{p_T^{t1} p_T^{t2}}$, of $R^{t1,t2}$ to $p_T^{t\bar{t}}$ and $|p_{\text{out}}|$; and of $|\cos\theta^*|$ and $\chi^{t\bar{t}}$ to $p_T^t/m^{t\bar{t}}$.

5.3 Shape comparison

We present a selection of variables shape comparisons for the 1B1S topology in this section. The most useful variable for searching for a resonant $t\bar{t}$ production is naturally the invariant mass of the $t\bar{t}$ system, $m^{t\bar{t}}$. The shape comparison show a clear peak for the vector (Z') as well as the scalar (y_0) models, see Figure 7. But shapes of other variables are also modified for such a signal, *e.g.* the top quark transverse momentum in Figure 10, exhibiting a broader peak rather than just a slope change. In contrast, the DM model leading to the associated production of a $t\bar{t}$ pair and a pair of DM particles ($\chi_D \bar{\chi}_D$) leads not only to an enhancement of the missing transverse energy where such a signal is often looked for, but also to a more prominent tail in the out-of-plane momentum distribution (p_{out}), see Figure 8. The spin of the resonance decaying to a pair of top quarks can be determined from the $\cos\theta^*$ distribution, as provided in Figure 9, as it leads to a slightly flatter spectrum for the scalar y_0 case but a more peaked shape for the case of a Z' production. Similar observations were found also in the 2B0S and 0B2S event topologies.

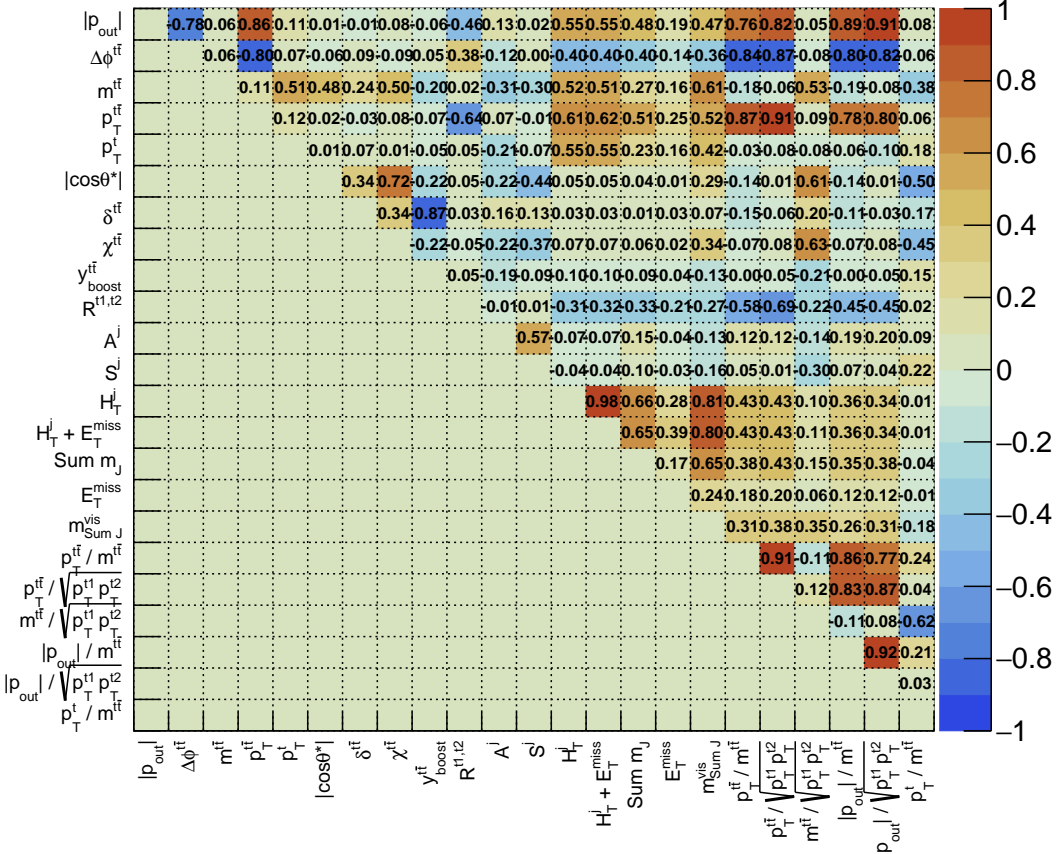
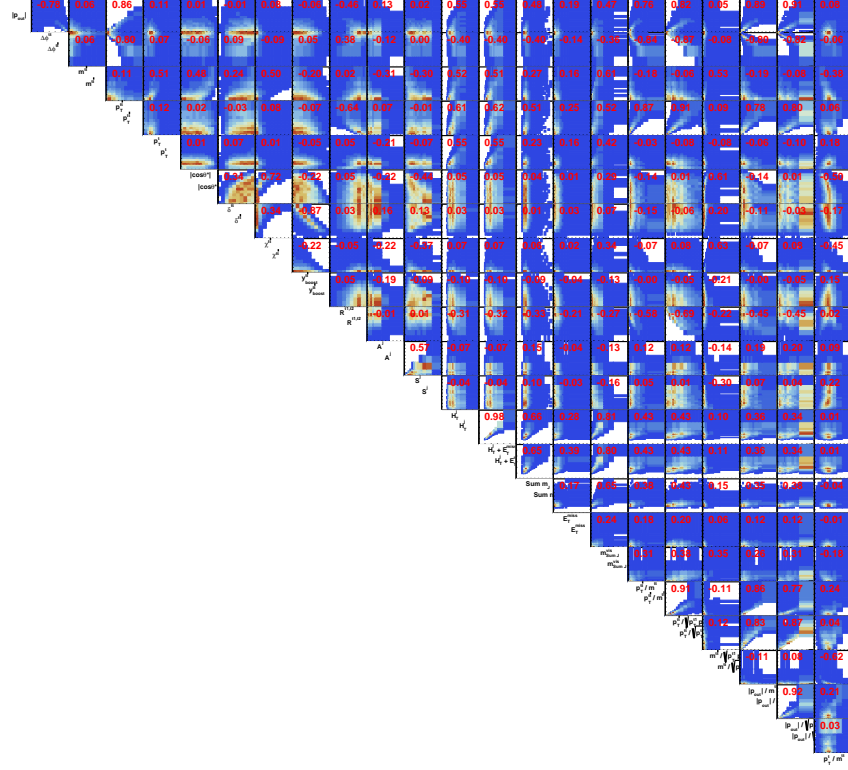


Figure 6. Example of correlations between kinematic variables at the detector level in the boosted-semiboosted (1B1S) topology evaluated on the $t\bar{t}$ control sample.

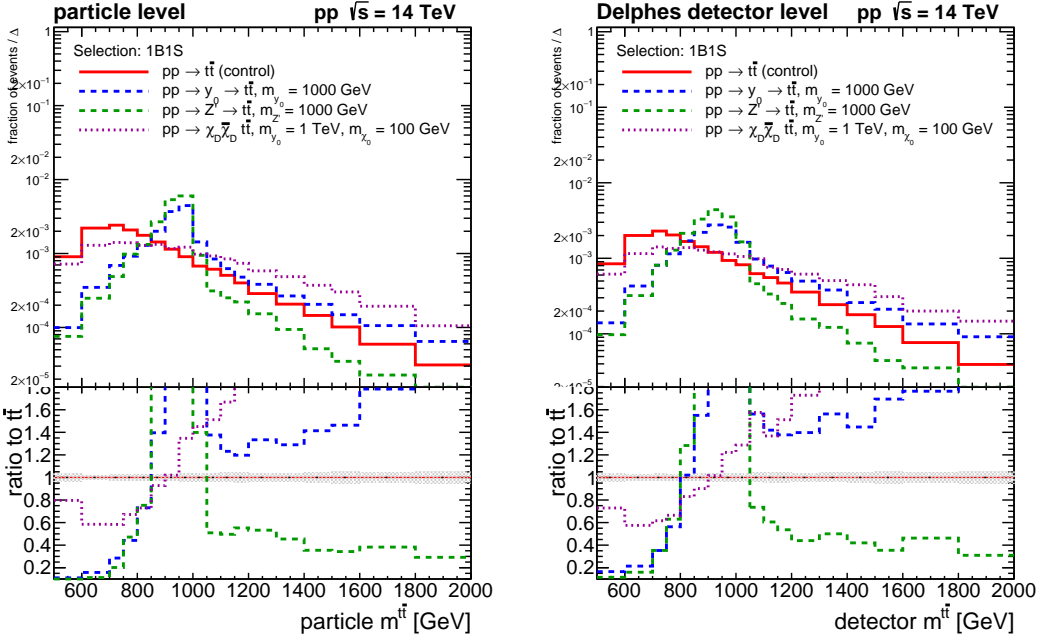


Figure 7. Shape comparison for the invariant mass of the $t\bar{t}$ pair in the boosted-semiboosted topology. Left: particle level, right: Delphes ATLAS detector level.

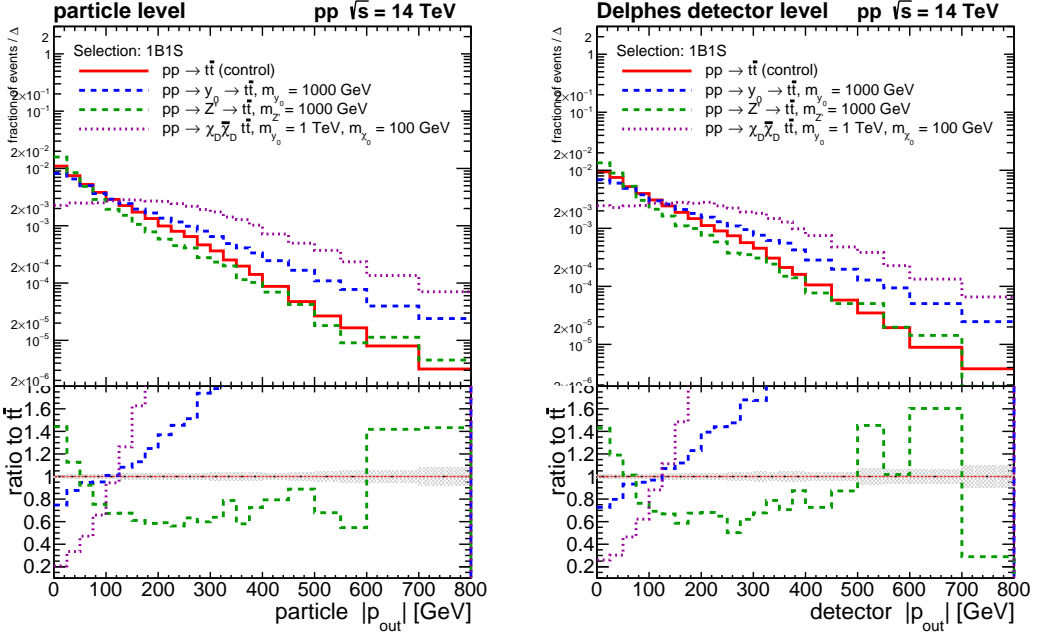


Figure 8. Shape comparison for the out-of-plane momentum p_{out} in the boosted-semiboosted topology. Left: particle level, right: Delphes ATLAS detector level.

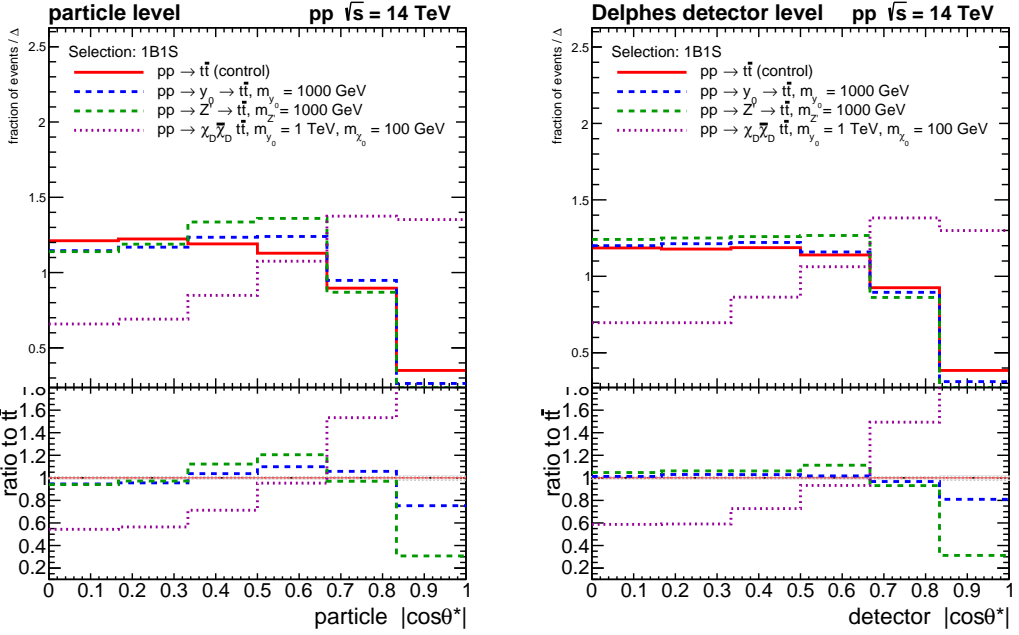


Figure 9. Shape comparison for the $\cos \theta^*$ in the boosted-semiboosted topology. Left: particle level, right: Delphes ATLAS detector level.

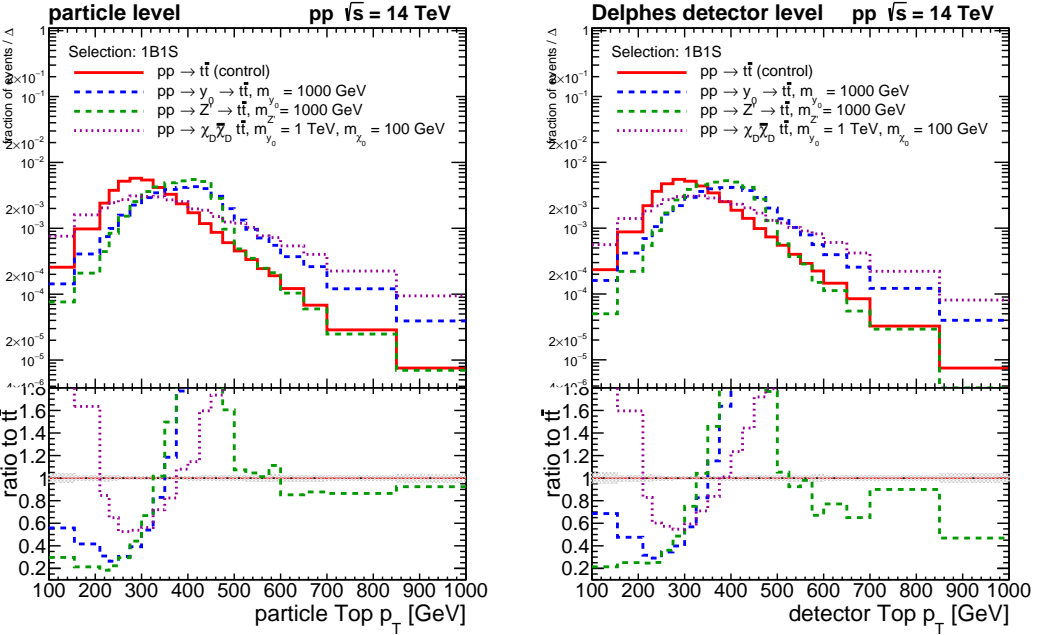


Figure 10. Shape comparison for the p_T of hadronic top quark candidate in the boosted-semiboosted topology. Left: particle level, right: Delphes ATLAS detector level.

6 Results

6.1 Pseudo-data study

For the purpose of creating a realistic mixed sample of a selected SM backgrounds (associated production of a W bosons and b -jets), the $t\bar{t}$ sample, as well as a new physics signal, detector-level distributions were created by mixing the samples based on their cross section σ using weights $w = \sigma L/N_{\text{gen}}$ (with L being the luminosity and N_{gen} the number of generated events with non-zero matching weights), but also scaling the signal in order to make it more prominent to study its shape and significance.

For the purpose of creating stacked plots consisting of physics and $t\bar{t}$ background and a selected signal model, the scalar y_0 model with the same mass was scaled by a factor of 12 and additional factors of $2^{1/2}$, $2^{3/2}$ and $2^{4.5}$ in the 2B0S, 1B1S and 0B2S topologies, respectively. Similarly, the Z' model with $m_{Z'} = 1000$ GeV was scaled by a factor of 10k, with additional $2^{1/2}$, 2^1 and 2^4 factors in the same topologies. The larger y_0 production cross section is partially due to the higher gluon-gluon parton luminosity in the production mechanism. Finally, the sample of the DM pair creation with associated $t\bar{t}$ production was scaled by a factor of 1k and additional factors of 2 in the 0B2S topology. The purpose of the additional scaling is to reach a similar level of signal significance across the topologies.

Examples of stacked samples forming predictions to the pseudo-data from the same but statistically independent samples showing a peaked $m^{t\bar{t}}$ and the $\chi^{t\bar{t}}$ variable distributions of signal for the y_0 model (Figure 11), a broader enhancement in terms of the top quark transverse momentum p_T^t and $p_T^{t\bar{t}}/m^{t\bar{t}}$ for the Z' model (Figure 12) are shown, together with the large signal in the tail of the $E_{\text{miss}}^{\text{miss}}$ distribution for the DM pair production (Figure 13).

6.2 Replicas

The technique of bootstrapping [28] is employed in order to construct statistically varied pseudo-independent versions (replicas) of 1D as well as 2D histograms, by repeatedly filling 100 replicas by events weighted by random weights drawn from the Poisson distribution of $\mu = 1$, *i.e.* as $w \sim \text{Poisson}(1)$. This ensures that every event is used in each replica once on average, and enables one to construct statistically correlated replicas across arbitrary histograms (projections) of any dimension over the events. The main aim is to evaluate signal excess over the replicas, obtaining a more robust estimator of the signal significance for each 1D or 2D spectrum in each topology and model.

6.3 Signal significance

The 1D significance of a signal over the total $t\bar{t}$ and non- $t\bar{t}$ background is evaluated at the detector level for scalar and vector resonant production of the $t\bar{t}$ pair as well as for the model of paired DM and $t\bar{t}$ production as $N_{\text{sig}}/\sqrt{\text{Var}_{\text{bg}} + \text{Var}_{\text{sig}}}$. In order to quantify the signal excess and find the most sensitive bin area, the 1D BUMPHUNTER algorithm [29] is employed, which finds the 1D window of a predefined size in which the probability of the data compatibility with the background-only hypothesis (p -value, p_{val}) is the smallest, constructing a test statistics $t \equiv -\log p_{\text{val}}^{\text{min}}$ which grows with the discrepancy. In detail, the p -value for the given area can be computed using the normalized incomplete gamma

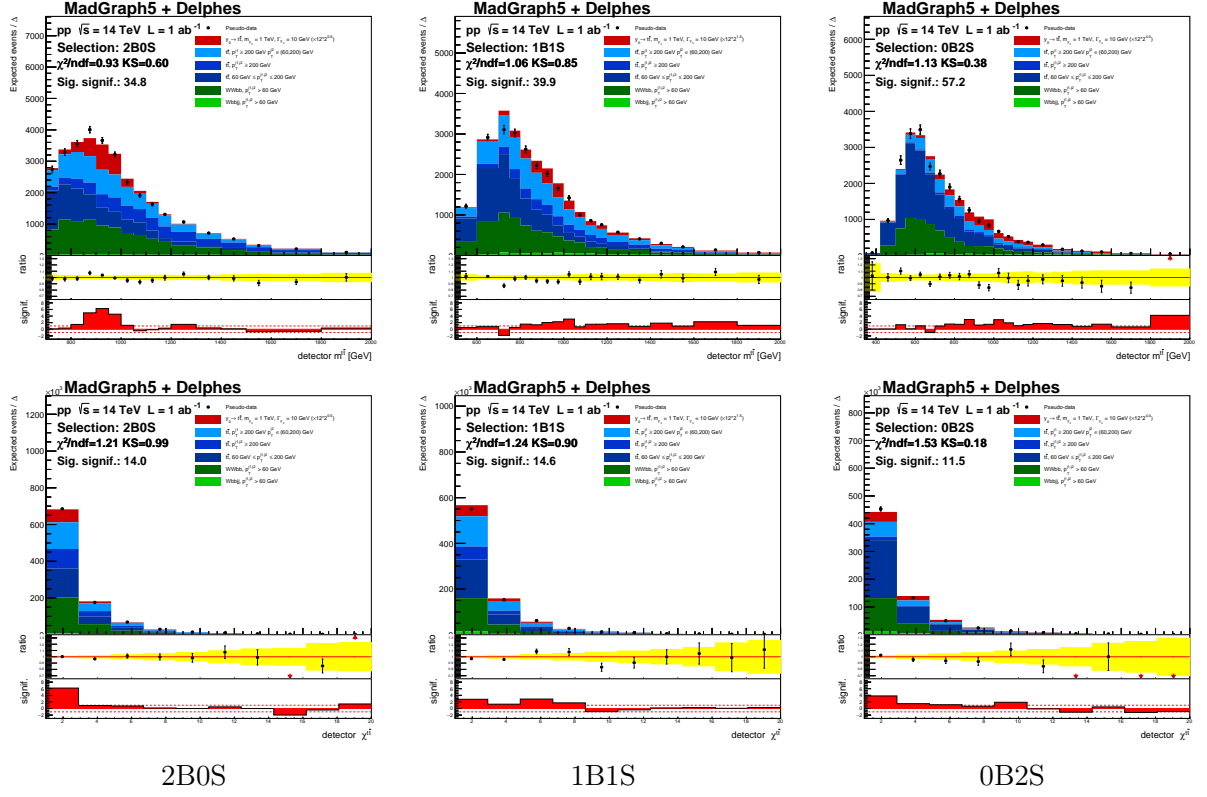


Figure 11. Stacked invariant mass of the $t\bar{t}$ pair (top) and the $\chi^{t\bar{t}}$ variable at the DELPHES detector level for the scaled y_0 model with $m_{y_0} = 1$ TeV, with both the pseudodata/prediction ratio and the signal significance shown in lower pads, for the boosted-boosted (2B0S, left), boosted-semiboosted (1B1S, middle) and semiboosted-semiboosted (0B2S, right) topologies. Also indicated are the χ^2 and Kolmogorov-Smirnov (KS) test statistics between the pseudo-data and predictions as provided by ROOT [27], and the total signal significance.

function as $\Gamma(d, b)$ for the case when the number of data events d is larger than the expected number of background events b , or as $1 - \Gamma(d + 1, b)$ otherwise, with

$$\Gamma(x, y) \equiv \frac{1}{\Gamma(x)} \int_0^y \zeta^{x-1} e^{-\zeta} d\zeta, \quad \Gamma(x) \equiv \int_0^\infty \zeta^{x-1} e^{-\zeta} d\zeta. \quad (6.1)$$

The function appears as a useful replacement for the sum of Poisson weight factors determining the probability of observing d events or more as the sum of Poisson terms for a distribution with mean b as ¹

$$\sum_{k=d}^{\infty} \frac{b^k}{k!} e^{-b} = \Gamma(d, b). \quad (6.2)$$

In our adaptation of the 1D BUMPHUNTER algorithm, the following constrains on the 1D area of interest are imposed, with the algorithm details outlined as follows:

¹There seems to be a typesetting mistake in Eq. 18 in [29] which should read $\sum_{n=d}^{\infty} \frac{b^n}{n!} e^{-b}$.

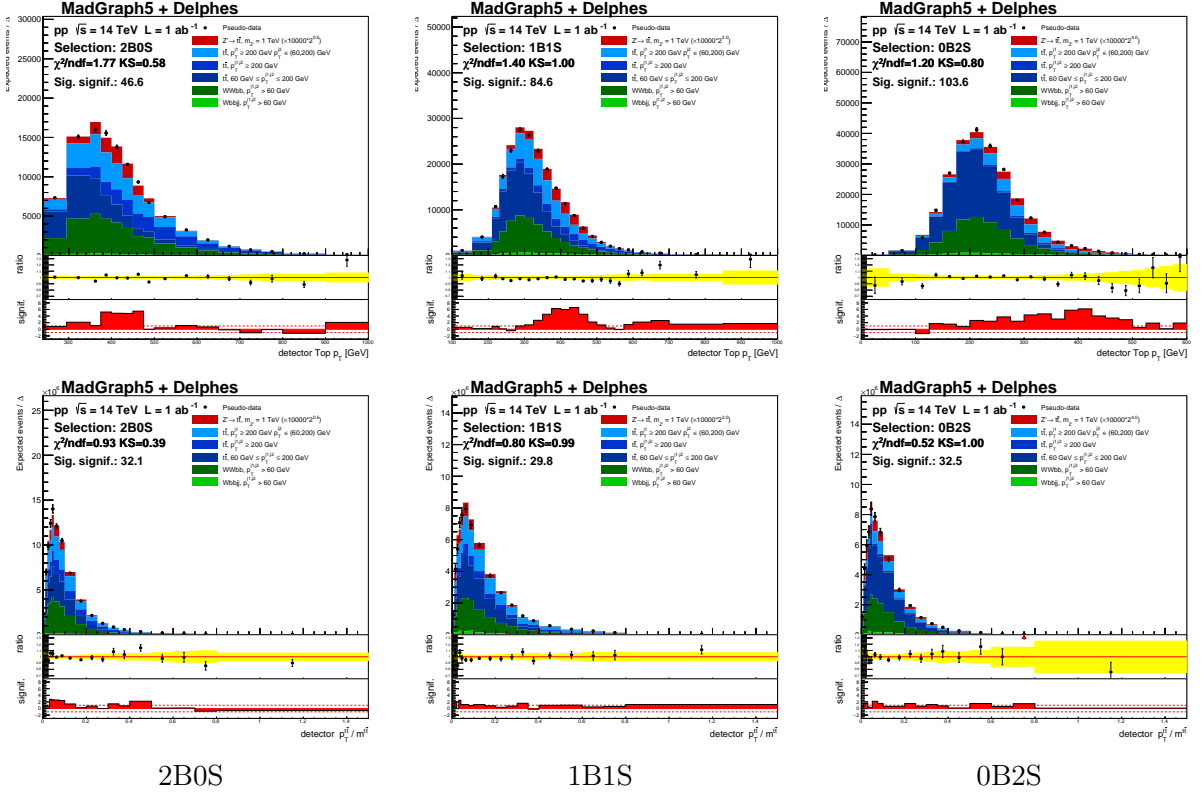


Figure 12. Stacked p_T of the reconstructed top quarks (top) and the $t\bar{t}$ pair p_T relative to the pair mass (bottom) at the DELPHES detector level for the scaled Z' model with $m_{Z'} = 1 \text{ TeV}$ with both the pseudodata/prediction ratio and the signal significance shown in lower pads, for the boosted-boosted (2B0S, left), boosted-semiboosted (1B1S, middle) and semiboosted-semiboosted (0B2S, right) topologies. Also indicated are the χ^2 and Kolmogorov-Smirnov (KS) test statistics between the pseudo-data and predictions as provided by ROOT [27], and the total signal significance.

- The initial 1D window width is 2 bins, starting with the window placed at the left of the spectrum.
- Compute the BUMPHUNTER test statistics t .
- Add the left- or right-neighbouring bin to the interval based on larger resulting t .
- Continue as long as the number of bins N of the interval under test in 1D fulfills $N \leq \frac{2}{3} n^{\text{bins}}$ where n^{bins} is the numbers of non-empty bins and as long as t grows.
- Start again with shifted search window by one bin from left to right.
- Try all such resulting 1D intervals, return the one with the best BH score.

We propose a natural 2D extension of the BUMPHUNTER algorithm following these considerations:

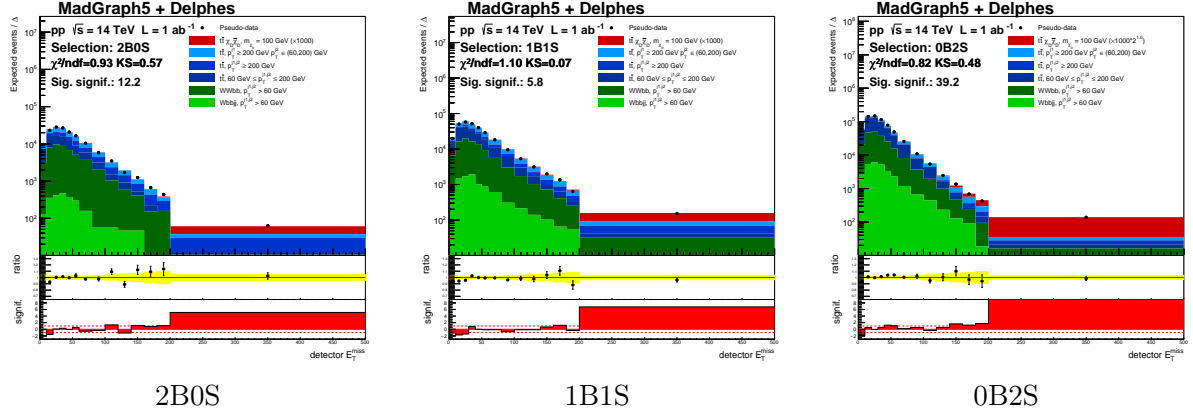


Figure 13. Stacked absolute value of the missing transverse energy at the DELPHES detector level for the scaled $y_0 \rightarrow \chi_D \bar{\chi}_D$, $m_{\chi_D} = 100$ GeV model with both the pseudodata/prediction ratio and the signal significance shown in lower pads, for the boosted-boosted (2B0S, left), boosted-semiboosted (1B1S, middle) and semiboosted-semiboosted (0B2S, right) topologies. Also indicated are the χ^2 and Kolmogorov-Smirnov (KS) test statistics between the pseudo-data and predictions as provided by ROOT [27], and the total signal significance.

- The initial 2D window width is 2×2 bins, placing the window at the bottom left of the spectrum.
- Compute the BUMPHUNTER test statistics t .
- Add a directly neighbouring bin to the current 2D area (excluding diagonal neighbours) which leads to the largest positive change in t .
- Continue as long as t grows and while the number of bins N of the 2D area under test its widths in x and y (w_x and w_y) fulfill $N < n^{\text{bins}} \wedge w_x \leq \frac{2}{3} n_x^{\text{bins}} \wedge w_y \leq \frac{2}{3} n_y^{\text{bins}}$, where n^{bins} is the numbers of non-empty bins and $n_{x,y}^{\text{bins}}$ are the number of non-empty bins of the 1D histogram projections along the x, y axes.
- Start again shifting the search window by one bin gradually in x and y directions from left to right.
- Try all such 2D areas, return the one with the best BH score.

For presentational purposes we further define the BH score as a logarithm of its test statistics, noting that a small shift in the score means a large shift in the actual BUMPHUNTER test statistics.

We present the 1D and 2D significances of signal over the expected background in corresponding histograms. The resulting histograms of the 1D and 2D BUMPHUNTER (BH) scores $\log t$ as well as the 2D histograms themselves for selected variables are shown in Figures 14–16, also with indicated 1D and 2D best BH areas. These are obtained by repeating the BUMPHUNTER procedure over the 100 statistically pseudo-independent replicas of the 1D and 2D spectra. The best discriminating variables in terms of the

BUMPHUNTER score for the three benchmark models are shown in Tables 3–5. It is observed that a single 1D variable never scores better than 2D variables.

Histograms of the score over all the variables are shown as 1D plots in Figures 17–19. In the 2D plots therein, the correlation coefficient for 253 studied 2D spectra built from 23 kinematic variables plotted as function of the best BH score, one can observe denser population of points within approximately $|\bar{\rho}| \lesssim 0.2$, but with a large spread. The $\bar{\rho}$ is the correlation coefficient averaged over 100 pseudo-experiments, computed using the $t\bar{t}$ control sample. One can conclude the small correlation is not the only property of two variables to possibly provide a stronger 2D signal significance than the individual 1D variables. Best variables exhibit a mixture of behaviour of those with small as well as large correlations, as well as negative correlations, sometimes negligible for SM $t\bar{t}$ but largely negative for signal, but in other cases also smaller positive correlation for signal.

Interestingly, for the y_0 and Z' models the $m^{t\bar{t}}$ variable is not the best standalone variable but is often preferred when paired with another variable, *e.g.* with H_T , E_T^{miss} , but also with jets sphericity or relative variables like $p_T^{t\bar{t}}/m^{t\bar{t}}$. Interestingly, the top quark p_T does not seem to help finding signal much, which may be regarded as a good news to worries of tuning new physics into physics models using this variable, while the transverse momentum of the $t\bar{t}$ system seems to be very sensitive (and harder to model). Other powerful variables turn out to be the sum of the large- R jet masses and the invariant mass of the 4-vector sum of large- R jets $m_{\sum J}^{\text{vis}}$, which has correlation of about 0.60 to $m^{t\bar{t}}$. Also the top quark p_T ratio variable $R^{t1,t2}$ vs. $m^{t\bar{t}}$ appears in the tables, as well as sphericity and aplanarity variables.

For the DM signal case, the best variable turns out to be E_T^{miss} in combination, as 2D variable, with $H_T + E_T^{\text{miss}}$. Although both variables are highly correlated (~ 1 for the $t\bar{t}$ and ~ 0.9 for the signal samples), the 2D histogram actually helps to separate the signal by moving it off the diagonal, leading to a large significance and 2D BH score. The signal scale factor for this model was chosen so that the 2D BUMPHUNTER significance for this variable is reasonable, which effectively reduced significances of all other variables to much smaller values. It was checked that besides the missing transverse energy, the best performing variables for the DM signal are similar to those for the Z' model, *e.g.* $p_T^{t\bar{t}}/m^{t\bar{t}}$, $p_T^{t\bar{t}}/\sqrt{p_T^{t1} p_T^{t2}}$, H_T^j , but also the p_{out} variable, which has a large correlation to $p_T^{t\bar{t}}$ ($\rho = 0.86$) but did not score prominently for the y_0 or Z' models. One can again think of this variable as a useful tuning rather than a search tool, or a proxy to $p_T^{t\bar{t}}$.

7 Conclusions

We present a realistic analysis of $t\bar{t}$ final states using SM and BSM samples and non- $t\bar{t}$ backgrounds corresponding to the integrated luminosity of 1 ab^{-1} , focusing on variables with potential to distinguish the signal of a resonant $t\bar{t}$ production or $t\bar{t}$ -associated DM pair production at the future LHC energy of 14 TeV.

The models with $t\bar{t}$ production mediated by a vector (Z') or scalar (y_0) predict the expected peak in the $t\bar{t}$ invariant mass in all studied 2B0S, 1B1S and 0B2S topologies. The

variable	2B0S	1B1S	0B2S
$\chi^{t\bar{t}}$ vs. $m^{t\bar{t}}$	5.06 ± 0.18		
E_T^{miss} vs. $H_T^j + E_T^{\text{miss}}$		5.02 ± 0.16	5.73 ± 0.14
E_T^{miss} vs. H_T^j		5.13 ± 0.16	5.73 ± 0.17
E_T^{miss} vs. $m^{t\bar{t}}$	5.17 ± 0.15		
E_T^{miss} vs. $\sum m^J$			5.59 ± 0.16
$H_T^j + E_T^{\text{miss}}$ vs. $\chi^{t\bar{t}}$		4.96 ± 0.21	
$H_T^j + E_T^{\text{miss}}$ vs. H_T^j		4.99 ± 0.19	5.56 ± 0.14
$H_T^j + E_T^{\text{miss}}$ vs. jets Sphericity		4.96 ± 0.2	
$H_T^j + E_T^{\text{miss}}$ vs. $m^{t\bar{t}}$	5.28 ± 0.14		
$H_T^j + E_T^{\text{miss}}$ vs. $y_{\text{boost}}^{t\bar{t}}$		4.98 ± 0.17	
H_T^j vs. $\chi^{t\bar{t}}$		4.92 ± 0.22	
H_T^j vs. jets Sphericity		4.99 ± 0.21	
H_T^j vs. $m^{t\bar{t}}$	5.26 ± 0.14		
H_T^j vs. $y_{\text{boost}}^{t\bar{t}}$		4.92 ± 0.18	
$m_{\sum J}^{\text{vis}}$ vs. E_T^{miss}		4.94 ± 0.19	5.53 ± 0.15
$m_{\sum J}^{\text{vis}}$ vs. $H_T^j + E_T^{\text{miss}}$		5.11 ± 0.17	5.69 ± 0.15
$m_{\sum J}^{\text{vis}}$ vs. H_T^j		5.07 ± 0.19	5.58 ± 0.16
$m_{\sum J}^{\text{vis}}$ vs. jets Sphericity		4.91 ± 0.22	
$m_{\sum J}^{\text{vis}}$ vs. $m^{t\bar{t}}$	5.1 ± 0.17		
$m^{t\bar{t}}/\sqrt{p_T^{t1}p_T^{t2}}$ vs. $m^{t\bar{t}}$	5.06 ± 0.18		
$p_T^{t\bar{t}}/m^{t\bar{t}}$ vs. E_T^{miss}		5.06 ± 0.18	5.64 ± 0.16
$p_T^{t\bar{t}}/m^{t\bar{t}}$ vs. H_T^j	5.03 ± 0.21	5.03 ± 0.19	
$p_T^{t\bar{t}}/m^{t\bar{t}}$ vs. $H_T^j + E_T^{\text{miss}}$	5.02 ± 0.23	5.01 ± 0.19	5.57 ± 0.13
$p_T^{t\bar{t}}/m^{t\bar{t}}$ vs. jets Sphericity		4.88 ± 0.23	
$p_T^{t\bar{t}}/m^{t\bar{t}}$ vs. $m_{\sum J}^{\text{vis}}$	5.04 ± 0.22	4.91 ± 0.23	
$p_T^{t\bar{t}}/m^{t\bar{t}}$ vs. $m^{t\bar{t}}$	5.12 ± 0.2		
$p_T^{t\bar{t}}/\sqrt{p_T^{t1}p_T^{t2}}$ vs. E_T^{miss}		4.95 ± 0.17	5.51 ± 0.17
$p_T^{t\bar{t}}/\sqrt{p_T^{t1}p_T^{t2}}$ vs. H_T^j		4.94 ± 0.18	
$p_T^{t\bar{t}}/\sqrt{p_T^{t1}p_T^{t2}}$ vs. $H_T^j + E_T^{\text{miss}}$		4.97 ± 0.18	
$p_T^{t\bar{t}}/\sqrt{p_T^{t1}p_T^{t2}}$ vs. $m_{\sum J}^{\text{vis}}$		4.95 ± 0.22	
$R^{t2,t1}$ vs. $m^{t\bar{t}}$	5.08 ± 0.17		
$\sum m^J$ vs. H_T^j		4.95 ± 0.17	
$\sum m^J$ vs. $H_T^j + E_T^{\text{miss}}$			5.55 ± 0.12
$\sum m^J$ vs. $m^{t\bar{t}}$	5.08 ± 0.16		

Table 3. The best 1D and/or 2D BUMPHUNTER variables scores ($\log t$) and the statistical uncertainty over 100 pseudo-experiments for the y_0 model with $m_{y_0} = 1$ TeV over the topologies. Empty fields indicate that the variable did not score within 1σ to the best scoring variable in given topology (red) while those scoring within 0.1σ are marked in bold.

model with $t\bar{t}$ -associated production of a pair of invisible pair of DM particles provide a broad excess in the $t\bar{t}$ mass in all considered topologies. All models predict a broad excess in top quark transverse momentum but also in other spectra. The addition of the semiboosted topologies into the selection can add about 10–15% events at the Z' mass of 1–1.5 TeV.

The 2D variable $H_T + E_T^{\text{miss}}$ versus the invariant mass of the 4-vector sum of large- R jets $m_{\sum J}^{\text{vis}}$ performs very well in terms of the signal significance. Other powerful variables are the $t\bar{t}$ rest frame angular variables like $\chi^{t\bar{t}}$, $y_{\text{boost}}^{t\bar{t}}$; or $\delta^{t\bar{t}}$ and relative dimensionless $p_T^{t\bar{t}}/m^{t\bar{t}}$, $p_T^{t\bar{t}}/m^{t\bar{t}}$ and $p_T^{t\bar{t}}/\sqrt{p_T^{t1}p_T^{t2}}$ which also exhibit a large signal significance potential while they also offer lower sensitivity to experimental uncertainties in the jet energy scale determination, being possibly more precise in real measurements. Especially simple yet

variable	2B0S	1B1S	0B2S
$\chi^{t\bar{t}}$ vs. $m^{t\bar{t}}$	5.13 ± 0.17		
E_T^{miss} vs. H_T^j		4.83 ± 0.18	
E_T^{miss} vs. $m^{t\bar{t}}$	5.24 ± 0.15	4.8 ± 0.23	
$H_T^j + E_T^{\text{miss}}$ vs. $\delta^{t\bar{t}}$		4.82 ± 0.22	
$H_T^j + E_T^{\text{miss}}$ vs. $m^{t\bar{t}}$	5.29 ± 0.15	4.94 ± 0.2	5.24 ± 0.29
H_T^j vs. $\delta^{t\bar{t}}$		4.85 ± 0.22	
H_T^j vs. $m^{t\bar{t}}$	5.29 ± 0.14	4.97 ± 0.19	5.32 ± 0.26
H_T^j vs. $p_T^{t\bar{t}}$		4.86 ± 0.18	
jets Aplanarity vs. $m^{t\bar{t}}$	5.17 ± 0.15		
jets Sphericity vs. $m^{t\bar{t}}$			5.29 ± 0.22
$m_{\sum J}^{\text{vis}}$ vs. $\Delta\phi^{t\bar{t}}$		4.9 ± 0.19	
$m_{\sum J}^{\text{vis}}$ vs. E_T^{miss}	5.15 ± 0.18	4.9 ± 0.19	5.28 ± 0.24
$m_{\sum J}^{\text{vis}}$ vs. H_T^j	5.16 ± 0.18	5.04 ± 0.18	5.31 ± 0.28
$m_{\sum J}^{\text{vis}}$ vs. $H_T^j + E_T^{\text{miss}}$	5.17 ± 0.18	5.04 ± 0.17	5.37 ± 0.25
$m_{\sum J}^{\text{vis}}$ vs. jets Aplanarity	5.26 ± 0.15		
$m_{\sum J}^{\text{vis}}$ vs. $m^{t\bar{t}}$	5.16 ± 0.17	4.88 ± 0.2	
$m_{\sum J}^{\text{vis}}$ vs. $p_T^{t\bar{t}}$	5.17 ± 0.18	4.94 ± 0.19	
$m_{\sum J}^{\text{vis}}$ vs. $R^{t2,t1}$	5.12 ± 0.19	4.9 ± 0.19	
$m_{\sum J}^{\text{vis}}$ vs. $\sum m^J$			4.82 ± 0.2
$m^{t\bar{t}}/\sqrt{p_T^{t1}p_T^{t2}}$ vs. H_T^j			5.23 ± 0.26
$m^{t\bar{t}}/\sqrt{p_T^{t1}p_T^{t2}}$ vs. $H_T^j + E_T^{\text{miss}}$			5.31 ± 0.22
$m^{t\bar{t}}/\sqrt{p_T^{t1}p_T^{t2}}$ vs. $m^{t\bar{t}}$	5.13 ± 0.17		
$m^{t\bar{t}}$ vs. $\Delta\phi^{t\bar{t}}$		5.21 ± 0.16	
$p_T^{t\bar{t}}/m^{t\bar{t}}$ vs. H_T^j	5.25 ± 0.2	5.08 ± 0.18	5.24 ± 0.24
$p_T^{t\bar{t}}/m^{t\bar{t}}$ vs. $H_T^j + E_T^{\text{miss}}$	5.18 ± 0.21	5.05 ± 0.18	5.21 ± 0.26
$p_T^{t\bar{t}}/m^{t\bar{t}}$ vs. $m_{\sum J}^{\text{vis}}$	5.36 ± 0.16	5.04 ± 0.2	5.23 ± 0.25
$p_T^{t\bar{t}}/m^{t\bar{t}}$ vs. $m^{t\bar{t}}$	5.35 ± 0.14	4.93 ± 0.21	5.32 ± 0.2
$p_T^{t\bar{t}}/\sqrt{p_T^{t1}p_T^{t2}}$ vs. E_T^{miss}			4.78 ± 0.28
$p_T^{t\bar{t}}/\sqrt{p_T^{t1}p_T^{t2}}$ vs. H_T^j	5.27 ± 0.23	5.06 ± 0.2	5.23 ± 0.25
$p_T^{t\bar{t}}/\sqrt{p_T^{t1}p_T^{t2}}$ vs. $H_T^j + E_T^{\text{miss}}$	5.27 ± 0.23	5.03 ± 0.19	5.23 ± 0.22
$p_T^{t\bar{t}}/\sqrt{p_T^{t1}p_T^{t2}}$ vs. $m_{\sum J}^{\text{vis}}$	5.3 ± 0.18	5.11 ± 0.22	5.34 ± 0.27
$p_T^{t\bar{t}}/\sqrt{p_T^{t1}p_T^{t2}}$ vs. $m^{t\bar{t}}$	5.3 ± 0.15	5.08 ± 0.18	5.51 ± 0.2
$p_T^{t\bar{t}}$ vs. $m^{t\bar{t}}$	5.21 ± 0.16	4.86 ± 0.21	5.22 ± 0.23
$p_T^{t\bar{t}}/m^{t\bar{t}}$ vs. p_T^t		5.01 ± 0.14	5.24 ± 0.23
$R^{t2,t1}$ vs. $m^{t\bar{t}}$	5.21 ± 0.16		
$\sum m^J$ vs. $m^{t\bar{t}}$	5.14 ± 0.16		

Table 4. The best 1D and/or 2D BUMPHUNTER variables scores ($\log t$) and the statistical uncertainty over 100 pseudo-experiments for the Z' model with $m_{Z'} = 1$ TeV over the topologies. Empty fields indicate that the variable did not score within 1σ to the best scoring variable in given topology (red) while those scoring within 0.1σ are marked in bold.

variable	2B0S	1B1S	0B2S
$H_T^j + E_T^{\text{miss}}$ vs. H_T^j	5.65 ± 0.11	5.84 ± 0.11	5.55 ± 0.11

Table 5. The best (2D) BUMPHUNTER variable score ($\log t$) and the statistical uncertainty over 100 pseudo-experiments for the DM $t\bar{t}$ -associated pair production $t\bar{t}\chi_D\bar{\chi}_D$ model with $m_{\chi_D} = 100$ GeV over the topologies.

powerful seems the signal separation for the $t\bar{t}$ -associated production of a pair of invisible DM particles in terms of the 2D distribution of E_T^{miss} vs. $H_T + E_T^{\text{miss}}$.

The proposed new 1D or 2D variables may prove useful for signal bump hunting in LHC searches or serve as input for a further usage in more involved classification approaches. While there do exist modern methods of identifying signal-enriched regions based on multivariate (MV) or machine learning (ML) techniques, the presented 2D BH algorithm may be regarded as a motivational intermediate stage for such more general classification schemes.

In conclusions, we identify statistically and systematics-robust variables with potential to enhance signal significance in sub-regions of these variables. The 2D BH studies lay between standard 1D and multivariate MV/ML techniques. The 2D variables offer a clear physics insight into regions which can be avoided to enhance signal significance. Also, such variables can be used as input to more powerful MV/ML classifiers.

Acknowledgments

The author would like to thank the Czech Science Foundation project GAČR 19-21484S for the support of this work.

References

- [1] Morad Aaboud et al. Search for heavy particles decaying into a top-quark pair in the fully hadronic final state in pp collisions at $\sqrt{s} = 13$ TeV with the ATLAS detector. *Phys. Rev.*, D99(9):092004, 2019.
- [2] Morad Aaboud et al. Search for heavy particles decaying into top-quark pairs using lepton-plus-jets events in proton-proton collisions at $\sqrt{s} = 13$ TeV with the ATLAS detector. *Eur. Phys. J.*, C78(7):565, 2018.
- [3] Albert M Sirunyan et al. Search for resonant $t\bar{t}$ production in proton-proton collisions at $\sqrt{s} = 13$ TeV. *JHEP*, 04:031, 2019.
- [4] Albert M Sirunyan et al. Search for a heavy resonance decaying to a top quark and a W boson at $\sqrt{s} = 13$ TeV in the fully hadronic final state. 4 2021.
- [5] J. Alwall, R. Frederix, S. Frixione, V. Hirschi, F. Maltoni, O. Mattelaer, H. S. Shao, T. Stelzer, P. Torrielli, and M. Zaro. The automated computation of tree-level and next-to-leading order differential cross sections, and their matching to parton shower simulations. *JHEP*, 07:079, 2014.
- [6] Duhr C. FeynRules Implementation of Abelian Higgs Model. 2011. <https://feynrules.irmp.ucl.ac.be/wiki/HiddenAbelianHiggsModel>.
- [7] Neil D. Christensen and Claude Duhr. FeynRules - Feynman rules made easy. *Comput. Phys. Commun.*, 180:1614–1641, 2009.
- [8] James D. Wells. How to Find a Hidden World at the Large Hadron Collider. 2008.
- [9] Stefan Hoeche, Frank Krauss, Nils Lavesson, Leif Lonnblad, Michelangelo Mangano, Andreas Schalicke, and Steffen Schumann. Matching parton showers and matrix elements. In *HERA and the LHC: A Workshop on the Implications of HERA for LHC Physics: CERN - DESY Workshop 2004/2005 (Midterm Meeting, CERN, 11-13 October 2004; Final Meeting, DESY, 17-21 January 2005)*, 2005.

[10] Torbjörn Sjöstrand, Stefan Ask, Jesper R. Christiansen, Richard Corke, Nishita Desai, Philip Ilten, Stephen Mrenna, Stefan Prestel, Christine O. Rasmussen, and Peter Z. Skands. An introduction to PYTHIA 8.2. *Comput. Phys. Commun.*, 191:159–177, 2015.

[11] Olivier Mattelaer and Eleni Vryonidou. Dark matter production through loop-induced processes at the LHC: the s-channel mediator case. *Eur. Phys. J. C*, 75(9):436, 2015.

[12] Mihailo Backović, Michael Krämer, Fabio Maltoni, Antony Martini, Kentarou Mawatari, and Mathieu Pellen. Higher-order QCD predictions for dark matter production at the LHC in simplified models with s-channel mediators. *Eur. Phys. J. C*, 75(10):482, 2015.

[13] Matthias Neubert, Jian Wang, and Cen Zhang. Higher-Order QCD Predictions for Dark Matter Production in Mono-Z Searches at the LHC. *JHEP*, 02:082, 2016.

[14] Goutam Das, Celine Degrande, Valentin Hirschi, Fabio Maltoni, and Hua-Sheng Shao. NLO predictions for the production of a spin-two particle at the LHC. *Phys. Lett. B*, 770:507–513, 2017.

[15] Sabine Kraml, Ursula Laa, Kentarou Mawatari, and Kimiko Yamashita. Simplified dark matter models with a spin-2 mediator at the LHC. *Eur. Phys. J. C*, 77(5):326, 2017.

[16] Andreas Albert et al. Recommendations of the LHC Dark Matter Working Group: Comparing LHC searches for dark matter mediators in visible and invisible decay channels and calculations of the thermal relic density. *Phys. Dark Univ.*, 26:100377, 2019.

[17] Chiara Arina, Mihailo Backović, Jan Heisig, and Michele Lucente. Solar γ rays as a complementary probe of dark matter. *Phys. Rev. D*, 96(6):063010, 2017.

[18] Y. Afik, F. Maltoni, K. Mawatari, P. Pani, G. Polesello, Y. Rozen, and M. Zaro. DM+ $b\bar{b}$ simulations with DMSimp: an update. In *Dark Matter at the LHC 2018: Experimental and theoretical workshop*, 11 2018.

[19] Thorsten Ohl. Drawing Feynman diagrams with Latex and Metafont. *Comput. Phys. Commun.*, 90:340–354, 1995.
<http://osksn2.hep.sci.osaka-u.ac.jp/~taku/osx/feynmp.html>.

[20] J. de Favereau, C. Delaere, P. Demin, A. Giannanco, V. Lemaître, A. Mertens, and M. Selvaggi. DELPHES 3, A modular framework for fast simulation of a generic collider experiment. *JHEP*, 02:057, 2014.

[21] Matteo Cacciari, Gavin P. Salam, and Gregory Soyez. FastJet User Manual. *Eur. Phys. J.*, C72:1896, 2012.

[22] David Krohn, Jesse Thaler, and Lian-Tao Wang. Jet Trimming. *JHEP*, 02:084, 2010.

[23] Andrew J. Larkoski, Simone Marzani, Gregory Soyez, and Jesse Thaler. Soft Drop. *JHEP*, 05:146, 2014.

[24] Stephen D. Ellis, Christopher K. Vermilion, and Jonathan R. Walsh. Recombination Algorithms and Jet Substructure: Pruning as a Tool for Heavy Particle Searches. *Phys. Rev. D*, 81:094023, 2010.

[25] Jesse Thaler and Ken Van Tilburg. Identifying Boosted Objects with N-subjettiness. *JHEP*, 03:015, 2011.

[26] Studies on top-quark Monte Carlo modelling for Top2016. Technical Report ATL-PHYS-PUB-2016-020, CERN, Geneva, Sep 2016.

- [27] I. Antcheva et al. ROOT: A C++ framework for petabyte data storage, statistical analysis and visualization. *Comput. Phys. Commun.*, 180:2499–2512, 2009.
- [28] Gerhard Bohm and Günter Zech. *Introduction to Statistics and Data Analysis for Physicists; 3rd revised.* Verlag Deutsches Elektronen-Synchrotron, Hamburg, 2017.
- [29] Georgios Choudalakis. On hypothesis testing, trials factor, hypertests and the BumpHunter. In *PHYSTAT 2011*, 1 2011.

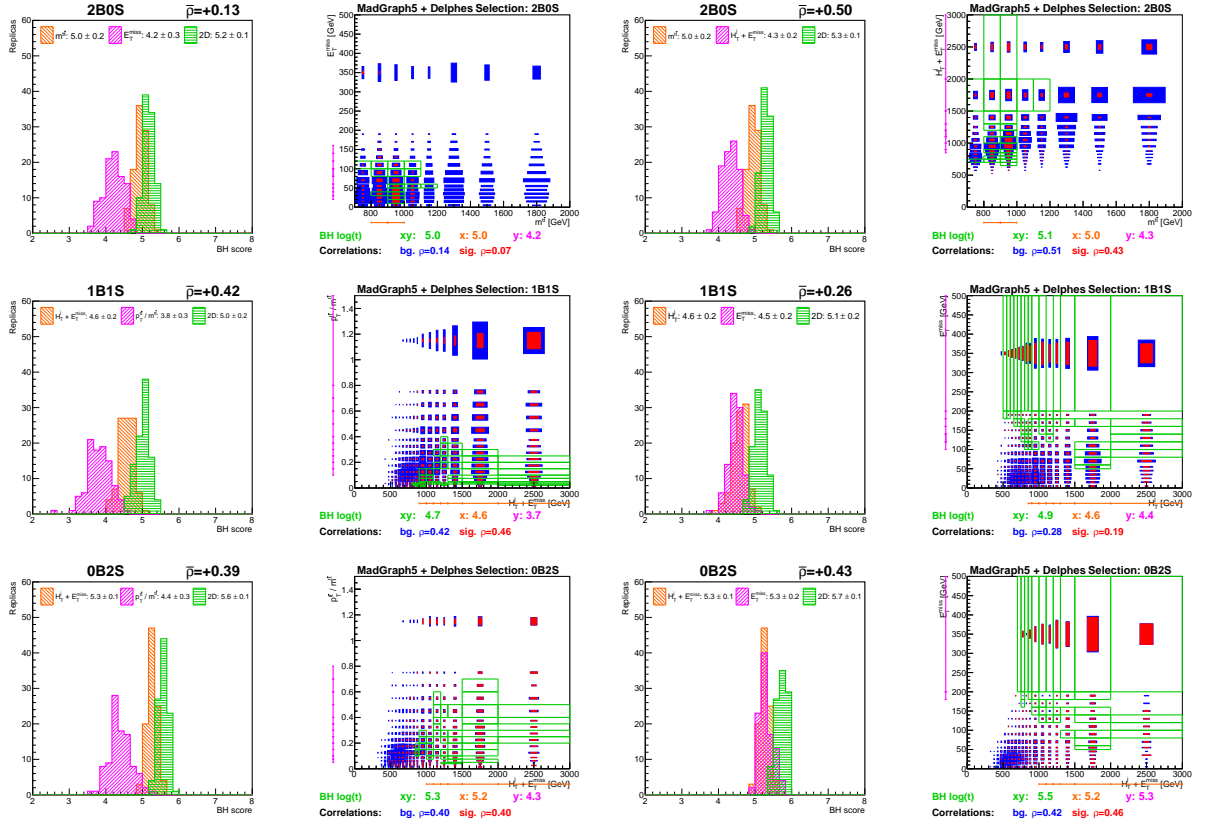


Figure 14. Best variables for the scalar y_0 model with $m_{y_0} = 1000$ GeV in the 2B0S (top), 1B1S (middle) and 0B2S (bottom) topologies. The green boxes indicate the best 2D (xy) BUMPHUNTER area while the vertical purple and horizontal orange bars indicate the bin ranges of the best 1D BUMPHUNTER areas for variables on the y and x axes, respectively. The blue (red) boxes area is proportional to the number of total signal+background (signal) events.

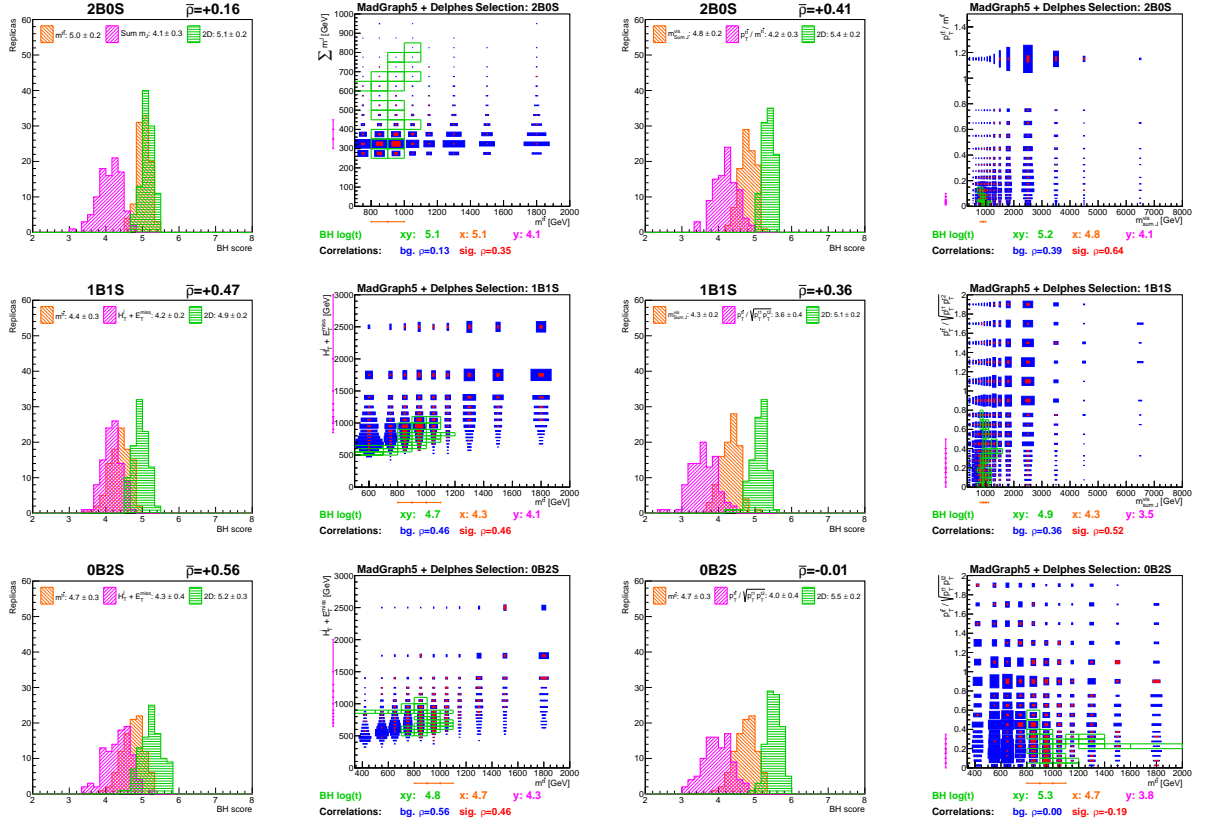


Figure 15. Best variables for the vector Z' model with $m_{Z'} = 1000$ GeV in the 2B0S (top), 1B1S (middle) and 0B2S (bottom) topologies. The green boxes indicate the best 2D (xy) BUMPHUNTER area while the vertical purple and horizontal orange bars indicate the bin ranges of the best 1D BUMPHUNTER areas for variables on the y and x axes, respectively. The blue (red) boxes area is proportional to the number of total signal+background (signal) events.

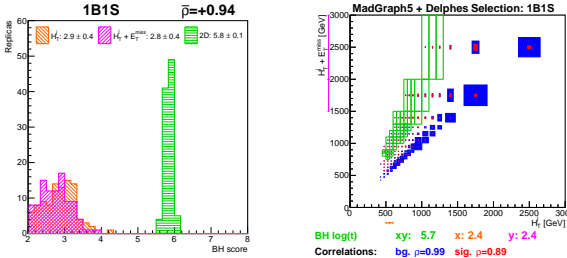


Figure 16. The best variable for the associated production of a $t\bar{t}$ pair with a pair of DM particles with $m_{\chi_D} = 100$ GeV in the 1B1S topology (the picture is very similar in the other topologies). The green boxes indicate the best 2D (xy) BUMPHUNTER area while the vertical purple and horizontal orange bars indicate the bin ranges of the best 1D BUMPHUNTER areas for variables on the y and x axes, respectively. The blue (red) boxes area is proportional to the number of total signal+background (signal) events.

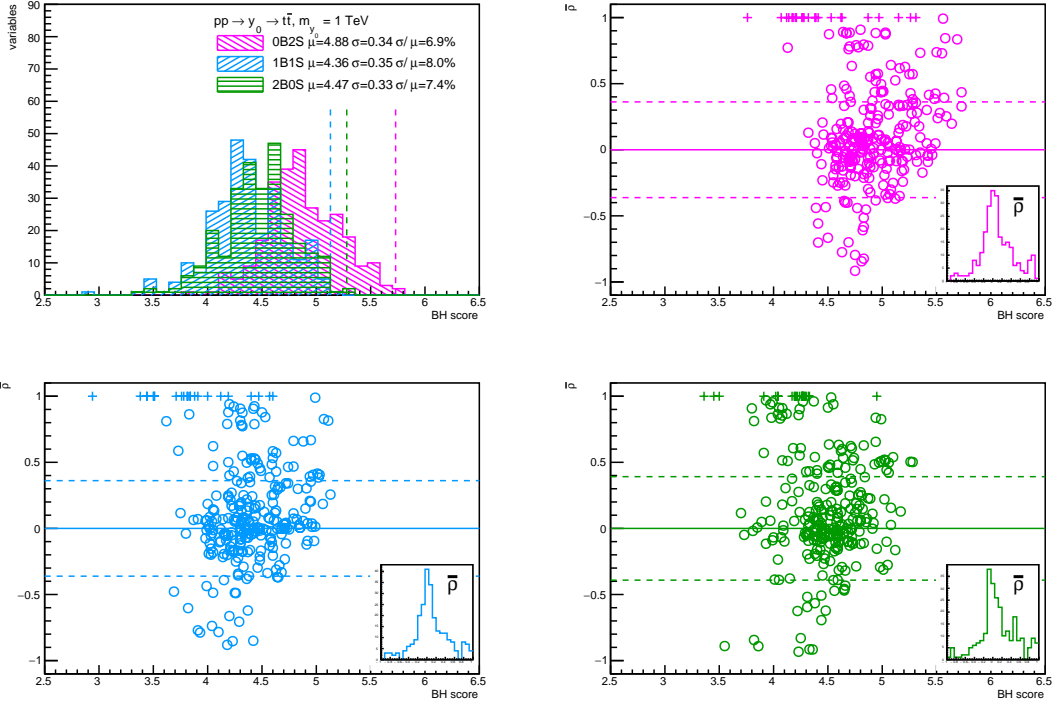


Figure 17. Mean BH scores over the variables for the scalar y_0 model with $m_{y_0} = 1000$ GeV (top left), the vertical dashed lines indicate more precisely the BH score for the best variable. In the 2D plots with the BH score on the x -axis and the correlation coefficient between two variables on the y -axis, the circle markers show the correlation vs. the 2D BH results while the crosses represent the 1D BH scores plotted at $\bar{\rho} = 1$. Green: the 2B0S, blue: 1B1S and pink: the 0B2S topologies. The insets shows the correlations distribution and the dashed horizontal guiding lines are drawn along $\pm\sigma_{\bar{\rho}}$, the correlations standard deviation over the studied 2D variables.

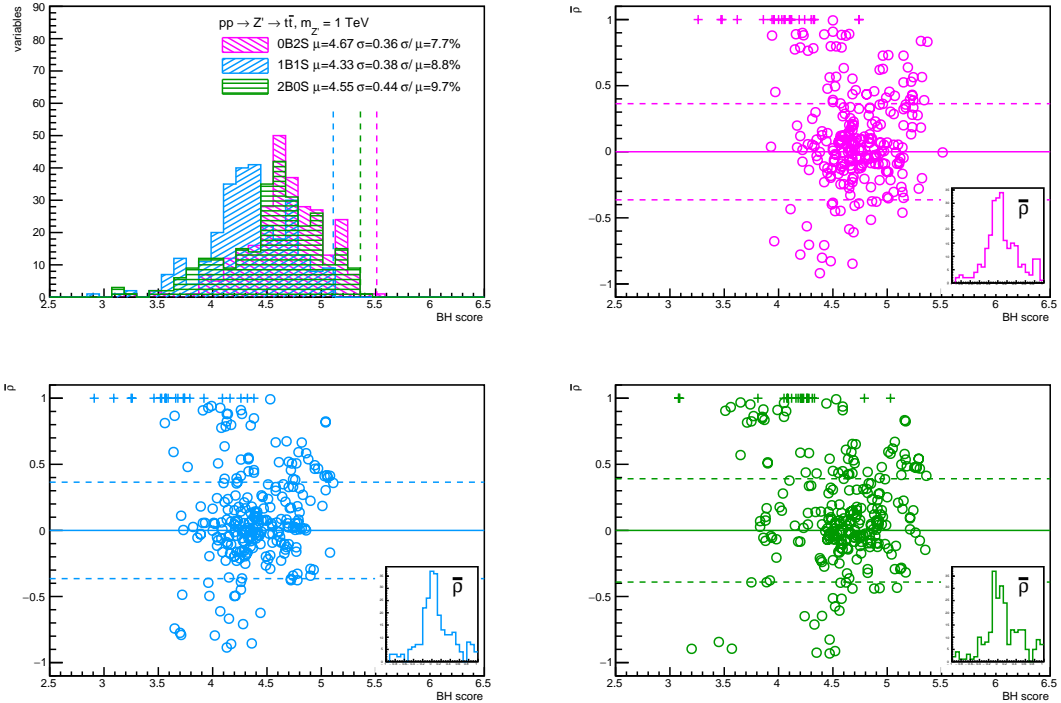


Figure 18. Mean BH scores over the variables for the vector Z' model with $m_{Z'} = 1000$ GeV (top left), the vertical dashed lines indicate more precisely the BH score for the best variable. In the 2D plots with the BH score on the x -axis and the correlation coefficient between two variables on the y -axis, the circle markers show the correlation vs. the 2D BH results while the crosses represent the 1D BH scores plotted at $\bar{\rho} = 1$. Green: the 2B0S, blue: 1B1S and pink: the 0B2S topologies. The insets shows the correlations distribution and the dashed horizontal guiding lines are drawn along $\pm\sigma_{\bar{\rho}}$, the correlations standard deviation over the studied 2D variables.

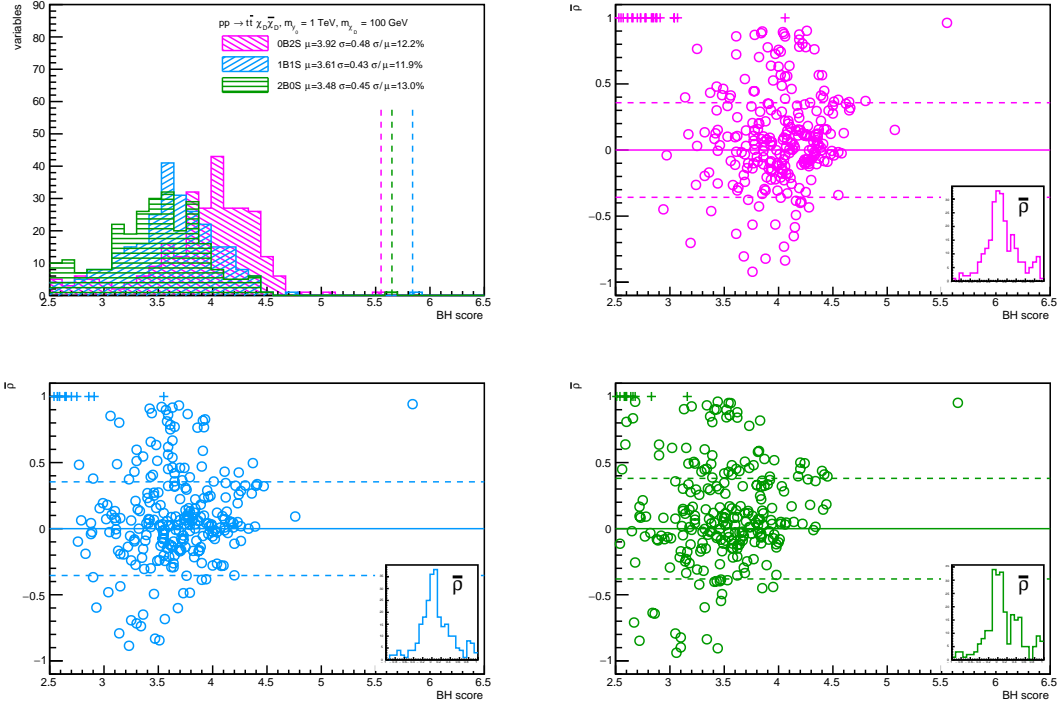


Figure 19. Mean BH scores over the variables for the associated production of $t\bar{t}$ with a pair of DM particles with $m_{\chi_D} = 100$ GeV (top left), the vertical dashed lines indicate more precisely the BH score for the best variable. In the 2D plots with the BH score on the x -axis and the correlation coefficient between two variables on the y -axis, the circle markers show the correlation vs. the 2D BH results while the crosses represent the 1D BH scores plotted at $\bar{\rho} = 1$. Green: the 2B0S, blue: 1B1S and pink: the 0B2S topologies. The insets shows the correlations distribution and the dashed horizontal guiding lines are drawn along $\pm\sigma_{\bar{\rho}}$, the correlations standard deviation over the studied 2D variables.